

The development of a bubble rising in a viscous liquid

By LI CHEN¹, SURESH V. GARIMELLA²,
JOHN A. REIZES³ AND EDDIE LEONARDI⁴

¹ Advanced Thermal-Fluid Technologies Laboratory, Division of Building, Construction and Engineering, CSIRO, P.O. Box 56, Highett, Victoria 3190, Australia
e-mail: li.chen@dbce.csiro.au

² Department of Mechanical Engineering, University of Wisconsin-Milwaukee,
Milwaukee, WI 53201, USA
e-mail: sureshg@uwm.edu

³ Faculty of Engineering, University of Technology, Sydney, Sydney 2007, Australia
e-mail: John.Reizes@uts.edu.au

⁴ School of Mechanical and Manufacturing Engineering, The University of New South Wales,
Sydney 2052, Australia
e-mail: E.Leonardi@unsw.edu.au

(Received 24 July 1997 and in revised form 16 November 1998)

The rise and deformation of a gas bubble in an otherwise stationary liquid contained in a closed, right vertical cylinder is investigated using a modified volume-of-fluid (VOF) method incorporating surface tension stresses. Starting from a perfectly spherical bubble which is initially at rest, the upward motion of the bubble in a gravitational field is studied by tracking the liquid–gas interface. The gas in the bubble can be treated as incompressible. The problem is simulated using primitive variables in a control-volume formulation in conjunction with a pressure–velocity coupling based on the SIMPLE algorithm. The modified VOF method used in this study is able to identify and physically treat features such as bubble deformation, cusp formation, breakup and joining. Results in a two-dimensional as well as a three-dimensional coordinate framework are presented. The bubble deformation and its motion are characterized by the Reynolds number, the Bond number, the density ratio, and the viscosity ratio. The effects of these parameters on the bubble rise are demonstrated. Physical mechanisms are discussed for the computational results obtained, especially the formation of a toroidal bubble. The results agree with experiments reported in the literature.

1. Introduction

Multi-fluid systems play an important role in many natural and industrial processes such as combustion, petroleum refining, chemical engineering and cleaning. Impressive developments in the visualization of fluid structure, detailed flow-field measurements, and sophisticated numerical simulations have led to significant progress in the understanding of complex single-phase flows in recent years. For flow that consists of two or more phases, however, difficulties are still encountered on both the experimental and numerical fronts. To fully understand the behaviour of a multi-fluid system the basic micro-mechanisms encountered in isolated fluid phases as well as the interactions

between multiple structures (e.g., bubbles) need to be satisfactorily characterized. A good overview of the subject may be found in Clift, Grace & Webes (1978).

The rise of bubbles in a liquid driven by a buoyancy force is one such multi-phase phenomenon. A sound understanding of the fundamentals of bubble rise is crucial in a variety of practical applications ranging from the rise of steam in boiler tubes to gas bubbles in oil wells. The rise of a bubble in a viscous liquid is accompanied by deformation of the bubble, resulting, in some cases, in a toroidal shape. A number of experimental studies have addressed this problem. For example, the rise of a bubble in an inviscid and a viscous liquid has been studied by Hartunian & Sears (1957), Walters & Davidson (1962, 1963), Wegener & Parlange (1973) and Bhaga & Weber (1981). Approximate theoretical solutions have been obtained in the limit of very small deformation for either high (Moore 1959) or low (Taylor & Acrivos 1964) Reynolds numbers. The fluid dynamics of the formation of a toroidal bubble is more complex, with compressibility, viscosity and surface-tension contributions expected to play a role (Best 1993).

In addition to being an interesting physical problem, the motion of a deforming bubble in a viscous liquid also represents a good example of an important class of free-boundary problems in fluid mechanics, from which a better understanding of both solution methods and the factors that control the boundary shape may be obtained.

The well-known analysis by Davies & Taylor (1950) of the rise of a spherical-cap bubble related the speed of rise to the radius of curvature of the bubble at the forward stagnation point, but the overall spherical-cap shape was assumed *a priori* rather than being determined as part of a full solution. Numerical simulations render possible the prediction of overall shape development of the bubble. Such numerical methods for solving problems with moving boundaries are discussed in an excellent review article by Floryan & Rasmussen (1989). Many computational studies in this area have been limited to the analysis of single drops and bubbles with small density ratios, in inviscid flow, and in two dimensions. Complications associated with the advection of the interfaces between two dissimilar fluids have largely limited numerical studies to simplified cases. The primary obstacle to effective simulation is the numerical diffusion which results in the sharpness of the advancing phase front being blurred, as well as the need for an accurate algorithm to solve for multiphase flow in the presence of highly discontinuous properties.

Amongst studies that have considered the deformation of a bubble in a liquid, Ryskin & Leal (1984) and Christov & Volkov (1985) investigated the steady-state deformation of a rising axisymmetric bubble over a range of Reynolds and Weber numbers using body-fitted coordinates. Claes & Leiner (1990) examined the rise of a single bubble using body-fitted coordinates without considering surface-tension effects. A two-dimensional bubble rising in an inviscid liquid was studied by Baker & Moore (1989) for a very small density ratio using the boundary-integral method, and by Anderson (1985) using the vortex method. Inviscid calculations (with the surface tension neglected) of a fully three-dimensional bubble at very low density ratios were carried out using a vortex-in-cell method by Brecht & Ferrante (1989). Recently, Unverdi & Tryggvason (1992a, b) studied the rise of two- and three-dimensional bubbles using a front tracking method, in which they represented the interface by an indicator function. An additional Eulerian grid was generated on the front which explicitly tracks the interface and moves through the stationary grid. A distribution function as in Peskin (1977) was used to exchange information between the interface and the stationary mesh: the velocities on the interface were obtained from the stationary

grid, and in return, the surface tension forces from the interface were transferred on to the grid. Inviscid, two-dimensional flow around deformable drops was investigated by Fyfe, Oran & Fritts (1988) using a moving triangular mesh in order to better represent the interface. Lafaurie *et al.* (1994) used a volume-tracking method, similar to the volume-of-fluid (VOF) method originally introduced by Hirt & Nichols (1981), to study the collision of three-dimensional drops in Cartesian coordinates. However, the discretization in this case was complicated due to the staggered mesh required as well as the difficulties in handling boundary conditions on pressure. The efficiency of the algorithm was also reduced by the explicit solutions adopted for the flow field.

There have also been studies in the literature that have investigated the formation of a toroidal bubble. Experimental observations of toroidal bubbles have been reported by Walters & Davidson (1963); very recently, Marten *et al.* (1996) studied ring bubbles generated by dolphins. Pedley (1968) presented an analytical solution to study the development of a toroidal bubble of regular shape in an inviscid flow, after its formation. Lundgren & Mansour (1991) used a boundary-integral method to study the deformation of a bubble from a spherical to a mushroom shape, as well as the development of a toroidal shape. The transition of the bubble from a sphere to a toroid had to be specified *a priori* to obtain a solution in their study. Best (1993) and Zhang, Duncan & Chahine (1993) attempted to improve this solution with their modified boundary-integral method to study the formation of a toroidal bubble formed upon the collapse of cavitation bubbles. Although these authors were able to simulate the flow before and after the toroid formation, the effects of viscosity and surface tension were not crucial in their work, and were neglected.

Of the multitude of approaches available for treating a moving interface, volume tracking has been chosen for this study due to its ease in specifying complex interfaces and treating three-dimensional interactions and merging/fragmenting. It may be noted that a level-set technique developed by Mulder, Osher & Sethian (1992) and Sussman, Smereka & Osher (1994) shares some characteristics with the volume-tracking method and may be discretized with any of the differencing schemes used for transport equations. But the difficulties in preventing numerical dissipation persist. It is difficult to neatly classify the increasing number of approaches to interface tracking in the literature, such as Lagrangian approaches including boundary-fitted grids (Ryskin & Leal 1984; Glimm, Marchesin & McBryan 1981; Duraiswami & Prosperetti 1992) and boundary-integral methods (Stone & Leal 1989), Eulerian approaches including volume-of-fluid (Hirt & Nichols 1981), level-set (Sethian 1996), phase-field (Murray Wheeler & Glicksman 1995), and enthalpy (Swaminathan & Voller 1993) methods; and mixed approaches (Unverdi & Tryggvason 1992a; Udaykumar, Shyy & Rao 1994); neither a classification nor a detailed review of interface-tracking methods is attempted here.

In this paper a method of solution is presented for the incompressible flow of two immiscible fluids, which accomplishes interface tracking through a modified VOF method with a semi-implicit algorithm on a non-staggered mesh. The solution is sought on the entire physical domain, thus avoiding the complexities and inaccuracies of implementing boundary conditions at an interface. The implementation of the algorithm presented is straightforward, even for three-dimensional flow. The problem is simulated using primitive variables ($\mathbf{u} - P$) in a control-volume formulation. The coupling of velocity and pressure is accomplished through the SIMPLE (Patankar 1980) algorithm. The primary focus of the present work is to elucidate the development of the shape of a single, isolated bubble from a sphere to a toroid, and the influence of various governing parameters on the shape development. An incompressible gas-

liquid system is considered with no phase change at the interface. Starting from a perfectly spherical bubble which is initially at rest, the upward motion of the bubble in a gravitational field is determined by tracking the liquid–gas interface. The results presented include two- and three-dimensional simulations incorporating the effects of surface-tension stresses at the interface modelled by the continuum surface force (CSF) model (Brackbill, Kothe & Zemach 1992). It may be noted that Magnaudet, Rivero & Fabre (1995) described the difficulties in simulating the motion of particles and bubbles, which lie in finding the appropriate governing equations for particle motion. In the model developed in the present work, this difficulty is overcome since the motion of the particle is indirectly solved by the advection of a local liquid volume fraction.

Multiple-bubble interactions, interactions of the bubbles with the container walls, and the effects of evaporation at the interface are treated in a separate paper (Chen *et al.* 1997).

2. Mathematical formulation

2.1. Governing equations

In this study, we investigate the rise of a bubble of gas in a cylindrical container of liquid. The velocity of the gas and liquid phases can be considered equal at the interface so that the velocity is continuous across the interface. Since the liquid is considered incompressible and fills the whole of the enclosure, and the container walls are rigid, the bubble volume—and hence the average density of the gas—must remain constant. The assumption of an isothermal system implies that the average pressure is also a constant. The gas in the bubble can be treated as incompressible, which greatly simplifies the analysis; the assumption was borne out by sample calculations of the pressure field in the gas. The incompressible Navier–Stokes equations may be used. In conservative and non-dimensional form, using

$$\begin{aligned} p^* &= \frac{p}{p_{ref}}, & \mathbf{U}^* &= \frac{\mathbf{U}}{u_{ref}}, & \mathbf{x}^* &= \frac{\mathbf{x}}{R_0}, \\ \tau &= \frac{t}{t_{ref}}, & \rho^* &= \frac{\rho}{\rho_{ref}}, & \mu^* &= \frac{\mu}{\mu_{ref}}, \\ \sigma^* &= \frac{\sigma}{\sigma_{ref}}, & u_{ref} &= (gR_0)^{1/2}, & p_{ref} &= \rho_{ref}u_{ref}^2, & t_{ref} &= \frac{u_{ref}}{R_0}, \end{aligned}$$

the Navier–Stokes equation may be expressed as

$$\frac{\partial(\rho\mathbf{U})}{\partial t} + \nabla \cdot (\rho\mathbf{U} \otimes \mathbf{U}) = -\nabla p + \frac{1}{Re}\nabla \times [\mu(\nabla\mathbf{U} + \nabla\mathbf{U}^T)] + \rho\mathbf{g} + \frac{1}{Bo}\mathbf{F}_{sv}, \quad (1)$$

$$\nabla \cdot \mathbf{U} = 0, \quad (2)$$

in which the superscript * is omitted for convenience, and \otimes denotes the outer product of tensors, $\mathbf{U} \equiv (u_r, u_\theta, u_z)$ is the fluid velocity in $\mathbf{x}(r, \theta, z)$, t the time, R_0 the initial bubble radius, σ the surface tension coefficient, ρ the density, μ the dynamic viscosity, p the pressure, \mathbf{g} the gravity vector, and \mathbf{F}_{sv} the volume form of the surface tension force (Brackbill *et al.* 1992). The Reynolds and Bond numbers are defined as

$$Re = \frac{\rho_f g^{1/2} R_0^{3/2}}{\mu_{ref}}, \quad Bo = \frac{\rho_f g R_0^2}{\sigma}$$

in which the subscripts f and ref denote liquid and reference properties respectively.

Although the uniform-density approximation is acceptable for an air–liquid system, it may not be true for a liquid–vapour system, especially if the interfacial phase-change process occurs rapidly. In this case, the interface propagation would be driven by an additional local velocity due to evaporation superimposed on the liquid flow field. Such a vapour–liquid situation is not considered in this paper; evaporation effects at the interface are considered in Chen *et al.* (1997).

In the gas–liquid system studied here, an initially stationary spherical bubble is considered with the initial condition

$$\mathbf{U}(t = 0) = \mathbf{0} \quad (3)$$

and with the boundary condition on the solid walls of the closed cylinder

$$\mathbf{U} = \mathbf{0}. \quad (4)$$

2.2. The interface description

Any discontinuous property equation could serve to represent interface transport. However, the ratio of the densities (or viscosities) for the water–air combination is so large, for example of the order of 1000 for densities and 100 for viscosities, that this sharp difference in values at the front complicates the simulation due to excessive numerical diffusion. This problem is overcome by using instead the volume fraction F , defined as the fraction of a control volume occupied by the liquid ($0 \leq F \leq 1$), to track the moving interface. Using the definition of the volume fraction, we represent the density and viscosity in the momentum equation as

$$\phi(\mathbf{x}, t) = F(\mathbf{x}, t)\phi_f + [1 - F(\mathbf{x}, t)]\phi_g, \quad (5)$$

where ϕ is either ρ or μ . The interface transport equation in terms of the F -function may be written as

$$\frac{\partial F}{\partial t} + (\mathbf{U} \cdot \nabla)F = 0. \quad (6)$$

which, when combined with the continuity equation, gives

$$\frac{\partial F}{\partial t} + \nabla \cdot (\mathbf{U}F) = F\nabla \cdot \mathbf{U}. \quad (7)$$

Including the divergence of velocity on the right-hand side helps prevent undershoots and overshoots in F and guarantees that the volume of a bubble is conserved. Since the F -function is used to track the interface instead of the discontinuity in density or viscosity, no additional smoothing is required. Equation (7) is solved by a modified Donor-Acceptor cell algorithm, as described later in this paper.

2.3. Surface-tension force

With the gradient of F chosen to represent the interface, the unit normal vector for the interface is given by

$$\hat{\mathbf{n}} = \frac{\nabla F}{|\nabla F|} \quad (8)$$

and the surface tension force by

$$\int_{A_i} \mathbf{F}_s dA = \int_{A_i} \sigma \kappa(\mathbf{x}_i) \hat{\mathbf{n}} dA \quad (9)$$

in which, \mathbf{F}_s , σ , κ and \mathbf{x}_i are the surface tension force, the coefficient of surface tension, the curvature of the interface, and its location respectively. In the CSF

model, a volume form of the surface tension can be written as

$$\int_{A_i} \mathbf{F}_s dA = \int_V \mathbf{F}_{sv} dV = \int_V \mathbf{F}_s \delta(\hat{\mathbf{n}} \cdot (\mathbf{x} - \mathbf{x}_i)) dV, \quad (10)$$

in which δ and its argument represent a delta function which is zero everywhere except at the interface $\mathbf{x}_i = (r_i, \theta_i, z_i)$. Since an interface having surface tension is being tracked with the VOF method, its topology will, in general, not be aligned with the logical mesh coordinates. The discontinuous interface is therefore represented in the computational domain as a finite-thickness transition region within which the fluid volume fraction varies smoothly from zero to one over a distance comparable to the computational mesh spacing. The volume form of the surface tension force, \mathbf{F}_{sv} , non-zero only within these transition regions, is given by (Brackbill *et al.* 1992)

$$\mathbf{F}_{sv}(\mathbf{x}, t) = \sigma \kappa(\mathbf{x}, t) \frac{\nabla F}{[F]}, \quad (11)$$

in which $[F]$, the jump in the value of F across the interface, is equal to unity in the present case. The term in (11) involving F represents a modified delta function. This form is not unique (see e.g. Mulder *et al.* 1992; Sussman *et al.* 1994; and Leveque & Li 1994 for other forms). As suggested by Brackbill *et al.* (1992), a smoother variation in κ generally results if a modified function F is used to calculate the surface normals in (11). A variety of smoothing algorithms (e.g. quadratic filter, Peskin's (1977) delta function) have been found to yield the desired result, but a slight smearing of the surface may occur. A better calculation of the curvature may be obtained using

$$\kappa(\mathbf{x}, t) = -(\nabla \cdot \hat{\mathbf{n}}). \quad (12)$$

Substituting for $\hat{\mathbf{n}}$ and expanding leads to

$$\kappa(\mathbf{x}, t) = \frac{1}{|\mathbf{n}|} \left[\left(\frac{\mathbf{n}}{|\mathbf{n}|} \cdot \nabla \right) |\mathbf{n}| - (\nabla \cdot \mathbf{n}) \right], \quad (13)$$

with $\mathbf{n} = \nabla F$. It is necessary to adopt a solution scheme to ensure that the net surface-tension force vanishes on a closed surface. This is discussed in § 3.1.

The problem is now fully specified and all that remains is to develop an appropriate solution procedure as discussed below.

3. Numerical method

Although the use of a staggered mesh can prevent oscillatory solutions of the pressure field, the discretization as well as the computations become more complicated as a result of its use. A non-staggered mesh with a suitable interpolation has been shown to overcome these difficulties, leading to a more robust computer code. A non-staggered mesh is used in this work with the Rhie & Chow (1983) interpolation to avoid oscillations in the pressure field. This simplifies the coding without loss of accuracy or the introduction of numerical instabilities. The computational domain has been divided into a number of non-overlapping control volumes such that one control volume surrounds each grid point, and all variables are defined at the centre of the control volume. The differential equations are integrated over each control volume. The discretization equations thus obtained express the conservation principle for all variables in the finite control volume, just as the original equations ensure conservation on infinitesimal control volumes. The pressure velocity coupling is accomplished through the SIMPLE algorithm with internal iteration.

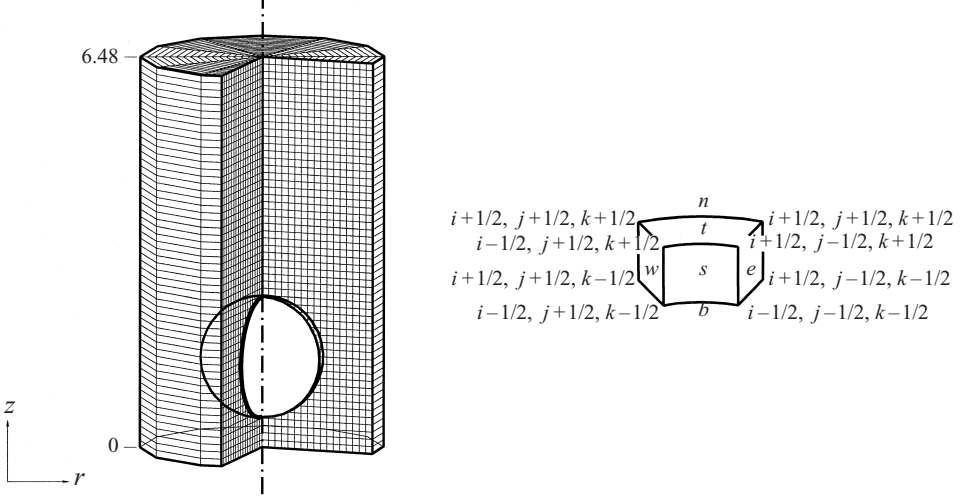


FIGURE 1. Schematic of the physical and computational domain and the control-volume notation in which the letters e, w, n, s, t , and b denote the faces of the control volume $P(i, j, k)$.

3.1. Discretization

All gradient terms in the discretized equations are central differenced, except for the convection terms which are treated through a hybrid scheme (Patankar 1980). Forward differencing is used to discretize the time-dependent terms (with $\Delta V_{i,j,k} = r_{i,j,k} \Delta r \Delta \theta \Delta z$)

$$\int_{\Delta V_{i,j,k}} \frac{\partial \phi}{\partial t} dV = \frac{\phi_{i,j,k}^{n+1} - \phi_{i,j,k}^n}{\Delta t} \Delta V_{i,j,k}. \quad (14)$$

The diffusion terms are integrated over the orthogonal control volume $P(i, j, k)$ (see figure 1 for control-volume notation) to give

$$\int_{\Delta V_{i,j,k}} \nabla \cdot (\Gamma \nabla \phi) dV = \int_{A_e} d_e dA - \int_{A_w} d_w dA + \int_{A_n} d_n dA - \int_{A_s} d_s dA + \int_{A_t} d_t dA - \int_{A_b} d_b dA \quad (15)$$

in which, for example, the diffusion term at the east face of the control volume is

$$\int_{A_e} d_e dA = D_e = \left(\Gamma \frac{\partial \phi}{\partial r} A \right)_e \quad (16)$$

and

$$\left(\frac{\partial \phi}{\partial r} \right)_e = \frac{\phi_{i+1,j,k} - \phi_{i,j,k}}{\Delta r}, \quad (17)$$

where ϕ denotes a variable, Γ is a diffusion coefficient, and A_e is the area of the east face of the control volume.

For an orthogonal grid, the integration of the convection terms yields

$$\begin{aligned} \int_{\Delta V_{i,j,k}} \nabla \cdot (\rho \mathbf{U} \phi) dV &= \int_{A_e} (f\phi)_e dA - \int_{A_w} (f\phi)_w dA + \int_{A_n} (f\phi)_n dA \\ &\quad - \int_{A_s} (f\phi)_s dA + \int_{A_t} (f\phi)_t dA - \int_{A_b} (f\phi)_b dA, \end{aligned} \quad (18)$$

in which, as an example, the flux of the variable ϕ on the east face of the control

volume is

$$\int_{A_e} (f\phi)_e dA = (\rho u_r \phi A)_e. \quad (19)$$

The hybrid scheme (Patankar 1980) is used to discretize ϕ and $u_{r,e}$ is obtained using Rhee & Chow's (1983) interpolation discussed in § 3.2 (equation (30)). If the cell Péclet number were greater than 2, it is believed that the hybrid scheme would be accurate only to the first order. However, even under conditions when the highest velocities are realized in the computational domain, more than 86% of cells have a local Péclet number of less than 2 for the problem studied in this paper. Therefore the scheme may be considered as second-order accurate in space.

The source terms, including the pressure and body force, are discretized as

$$\int_{\Delta V_{i,j,k}} s dV = (s \Delta V)_{i,j,k} = S_{i,j,k}. \quad (20)$$

This assumes that $S_{i,j,k}$ is piecewise uniform over each control volume.

As stated in Brackbill *et al.* (1992), a wide stencil in general leads to a better estimate for curvature. However, Rider *et al.* (1995) suggest that a conservative discretization of the curvature should be used due to the need to preserve an important physical property of the surface tension force, namely that the net normal surface tension force should vanish over any closed surface. In a test case which simulated an equilibrium bubble in a zero gravitational field using the discretization scheme suggested by Brackbill *et al.*, no unphysical result was obtained after 1000 time steps. We found that conventional central differencing leads to results which are similar to those with a discretization involving a wider stencil. The divergence of the normal vector in (13) is given by

$$\nabla \cdot \mathbf{n}_{i,j,k} = \left(\frac{n_r}{r} \right)_{i,j,k} + \left(\frac{\partial n_r}{\partial r} \right)_{i,j,k} + \frac{1}{r_{i,j,k}} \left(\frac{\partial n_\theta}{\partial \theta} \right)_{i,j,k} + \left(\frac{\partial n_z}{\partial z} \right)_{i,j,k}. \quad (21)$$

The use of (13) to determine the curvature requires the evaluation of

$$\begin{aligned} \left[\left(\frac{\mathbf{n}}{|\mathbf{n}|} \cdot \nabla \right) |\mathbf{n}| \right]_{i,j,k} &= \left(\frac{n_r}{|\mathbf{n}|} \right)_{i,j,k} \left(\frac{\partial |\mathbf{n}|}{\partial r} \right)_{i,j,k} \\ &\quad + \frac{1}{r_{i,j,k}} \left(\frac{n_\theta}{|\mathbf{n}|} \right)_{i,j,k} \left(\frac{\partial |\mathbf{n}|}{\partial \theta} \right)_{i,j,k} + \left(\frac{n_z}{|\mathbf{n}|} \right)_{i,j,k} \left(\frac{\partial |\mathbf{n}|}{\partial z} \right)_{i,j,k}. \end{aligned} \quad (22)$$

The gradients in the above equations are evaluated from the values at the faces of the control volume. For example,

$$\left(\frac{\partial |\mathbf{n}|}{\partial r} \right)_{i,j,k} = \frac{1}{\Delta r} (|\mathbf{n}|_e - |\mathbf{n}|_w) \quad (23)$$

gives the gradient of the magnitude of the normal vector. Its value on the faces of the control volume is obtained from a linear interpolation of the corner values.

$$\left. \begin{aligned} |\mathbf{n}|_e &= \frac{1}{4} (|\mathbf{n}|_{i+1/2,j-1/2,k-1/2} + |\mathbf{n}|_{i-1/2,j-1/2,k-1/2} + |\mathbf{n}|_{i-1/2,j-1/2,k+1/2} \\ &\quad + |\mathbf{n}|_{i+1/2,j-1/2,k+1/2}) \\ |\mathbf{n}|_w &= \frac{1}{4} (|\mathbf{n}|_{i+1/2,j+1/2,k-1/2} + |\mathbf{n}|_{i+1/2,j+1/2,k+1/2} + |\mathbf{n}|_{i-1/2,j+1/2,k+1/2} \\ &\quad + |\mathbf{n}|_{i-1/2,j+1/2,k-1/2}). \end{aligned} \right\} \quad (24)$$

The magnitude of the normal vector at the corners is calculated as

$$\begin{aligned} |\mathbf{n}|_{i+1/2,j+1/2,k+1/2} &= \left(n_{r,i+1/2,j+1/2,k+1/2}^2 + \left(\frac{n_\theta}{r} \right)_{i+1/2,j+1/2,k+1/2}^2 + n_{z,i+1/2,j+1/2,k+1/2}^2 \right)^{1/2} \end{aligned} \quad (25)$$

for the corner $(i + 1/2, j + 1/2, k + 1/2)$ of the cell (i, j, k) , etc.

The r -direction component of the normal vector at the centre of the control volume $P(i, j, k)$ is calculated as the average of the values at the corners:

$$\begin{aligned} n_{r,i,j,k} = \left(\frac{\partial F}{\partial r} \right)_{i,j,k} &= \frac{1}{8} \left[\left(\frac{\partial F}{\partial r} \right)_{i+1/2,j+1/2,k+1/2} + \left(\frac{\partial F}{\partial r} \right)_{i-1/2,j+1/2,k+1/2} \right. \\ &\quad + \left(\frac{\partial F}{\partial r} \right)_{i+1/2,j-1/2,k+1/2} + \left(\frac{\partial F}{\partial r} \right)_{i-1/2,j-1/2,k+1/2} \\ &\quad + \left(\frac{\partial F}{\partial r} \right)_{i+1/2,j+1/2,k-1/2} + \left(\frac{\partial F}{\partial r} \right)_{i-1/2,j+1/2,k-1/2} \\ &\quad \left. + \left(\frac{\partial F}{\partial r} \right)_{i+1/2,j-1/2,k-1/2} + \left(\frac{\partial F}{\partial r} \right)_{i-1/2,j-1/2,k-1/2} \right], \end{aligned} \quad (26)$$

in which

$$\begin{aligned} n_{r,i+1/2,j+1/2,k+1/2} &= \left(\frac{\partial F}{\partial r} \right)_{i+1/2,j+1/2,k+1/2} = \frac{1}{4\Delta r} [F_{i+1,j+1,k+1} - F_{i,j+1,k+1} \\ &\quad + F_{i+1,j,k+1} - F_{i,j,k+1} + F_{i+1,j+1,k} - F_{i,j+1,k} + F_{i+1,j,k} - F_{i,j,k}] \end{aligned} \quad (27)$$

is the r -direction component at the corner $(i + 1/2, j + 1/2, k + 1/2)$ of the control volume. It may be seen that the discretization of (13) is very complex. Only seven grid points are required, instead, if one uses (12), thus leading to a simpler discretization.

3.2. The final form

Using the above discretizations of the governing equations, a form ready for solution is obtained, namely

$$\phi_P = \frac{\sum(a_{N,P}\phi_{N,P}) + S_P}{a_P}, \quad (28)$$

in which N indicates the neighbouring points surrounding $P(i, j, k)$ and coefficients $a_{N,P}$ involve the flow properties of convection, diffusion, and area; details may be found in Patankar (1980).

As previously mentioned, in order to prevent oscillations in the pressure field the Rhee & Chow (1983) interpolation, which naturally relates the velocity of the control volume to the pressure difference between neighbouring nodes, is used. To implement this interpolation, the momentum equation is rewritten as

$$\mathbf{U}_P = \frac{\sum a_{N,P} \mathbf{U}_{N,P} + S_P}{a_P} - (B\nabla_p)_P, \quad (29)$$

in which $B = (\Delta V/a_P)$ and S_P is the source term with the pressure gradient excluded. For example, the Rhee & Chow interpolation for the velocity in the r -direction on the east face of the control volume $P(i, j, k)$ may be written as

$$u_{r,e} = w_e \Psi_{r,i,j,k} + (1-w_e) \Psi_{r,i,j,k} - [w_e B_{i,j,k} + (1-w_e) B_{i+1,j,k}] \left(\frac{1}{\Delta r} (P_{i+1,j,k} - P_{i,j,k}) \right), \quad (30)$$

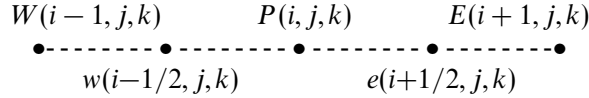
in which

$$\Psi_{r,i,j,k} = \frac{\sum a_{N,i,j,k} u_{r,N,i,j,k} + S_{i,j,k}}{a_{i,j,k}}. \quad (31)$$

In these equations, subscript r refers to the component in the r -direction, and w_e is a geometric weighting factor which is dependent on the location of the cell surface and is given by

$$w_e = \frac{\overline{Pe}}{\overline{Pe} + e\overline{E}}$$

if the grid is arranged as



3.3. Pressure–velocity coupling

Conventionally, the VOF method for interface tracking uses the same approach to coupling velocity and pressure as the MAC method (Welch *et al.* 1966), in which boundary conditions on the pressure have to be explicitly specified. This approach is prone to problems associated with outflow boundary conditions as well as those in the governing equations caused by the staggered mesh typically used. This problem is circumvented in the present work, where the SIMPLE algorithm is used: a direct solution of the pressure equation is avoided, making the simulation more robust. In addition, a non-staggered mesh is used in this work to reduce the level of complexity of the solution. The coupling algorithm is briefly explained in the following. Equation (29) for the point $P(i, j, k)$ may be rewritten in discretized form as

$$\mathbf{U}_P^* = \frac{\mathbf{H}_P^*}{a_P} - (B\nabla p)_P, \quad (32)$$

in which

$$\mathbf{H}_P^* = \sum a_{N,P} \mathbf{U}_{N,P}^* + \mathbf{S}_P^n$$

and superscript * denotes intermediate values of the variables. If an improved pressure field and a corresponding velocity field could be defined such that

$$P_P^{**} = P_P^* + P'_P, \quad \mathbf{U}_P^{**} = \mathbf{U}_P^* + \mathbf{U}'_P, \quad (33)$$

then, substituting (33) into (32) and subtracting the resultant expression from (32) leads to

$$\mathbf{U}'_P = \frac{\mathbf{H}'_P}{a_P} - (B\nabla p')_P. \quad (34)$$

Ignoring the first term on the right-hand side in (34), we have for the velocity correction

$$\mathbf{U}'_P = -(B\nabla p')_P. \quad (35)$$

The continuity equation (2) at any point can then be written upon substitution of (33) and (35) as

$$\nabla \cdot \left[\left(\frac{\rho \Delta V}{\Delta t} - A_0 \right)^{-1} \nabla p' \right] = \nabla \cdot \mathbf{U}^*. \quad (36)$$

The iteration process is continued until $\nabla \cdot \mathbf{U}^* \rightarrow 0$, at which stage a converged solution is obtained. It is realized that the neglect of the first term on the right-hand

side of (33) results in an exaggerated pressure field. The pressure is updated partially during the solution procedure using a relaxation factor so that no accumulation of error occurs as demonstrated by Patankar (1980). In addition, for the pressure correction equation, we have the boundary condition

$$\nabla p' \cdot \hat{\mathbf{n}}_c = 0 \quad (37)$$

due to the fact that the velocities have been specified to satisfy the continuity at the corresponding boundary and no correction is needed. It is understood that the use of this algorithm ensures that the face velocities satisfy continuity; this need not necessarily be true for the velocities at the centre of a control volume.

The most computationally expensive portion of the algorithm is the solution of the linear system of equations arising from the discretization of the momentum and pressure equations, especially the Poisson equation for pressure correction. Moreover, the large difference in magnitudes of the coefficient matrix of (36) caused by the sharp jump in density across the interface cell introduces additional difficulties into the solution. A direct solution is computationally prohibitively expensive; traditional iterative techniques are equally expensive in terms of the number of operations performed (the operation-count scales with the square of the number of the number of equations for standard methods like SOR), although they are cheaper in terms of storage. The symmetric system of equations (36) for the pressure correction allowed a Preconditioned Conjugate Gradient (ICCG(0)) algorithm (Meijerink & van der Vorst 1977) to be used. For the non-symmetric set of equations for momentum (29), a Preconditioned Bi-Conjugate-Gradient-Stable method along with a Stone implicit procedure (SIP) due to Stone (1968) was the approach chosen. In this algorithm, the incomplete Choleski decomposition, IC(0), was used as the preconditioner.

3.4. Implementation of the interface tracking (VOF)

Previous work on volume tracking has been done using SLIC (Noh & Woodward 1976) and VOF methods, in which all underlying equations were solved on a fixed Eulerian mesh. However, some improvements to the original algorithm were necessary in order to obtain more accurate results in the present work. In tracking the volume function F two issues arise: identifying the exact location of the interface i.e. reconstructing the interface at each time step), and advecting it. The original VOF approach (Hirt & Nichols 1981) developed for two-dimensional flow in Cartesian coordinates adopted a simplified distance function to reconstruct the interface, and a donor-acceptor algorithm to advect it. The donor-acceptor technique appears to succeed in preventing a smearing of the interface; however, the reconstruction of the interface is very rough, and is also coordinate-system dependent. Partom (1987) used the VOF method to calculate inviscid three-dimensional free-surface flow in a cylinder. It appears that some great simplifications may have been devised, but this cannot be established since details of the implementation were not reported. Some attempts at improving the reconstruction of the interface are reported in Chorin (1985) to study the problem of solidification in two dimensions and by Sethian (1985) in a body-fitted coordinate system.

Youngs (1982, 1984) modified the original VOF method to study an unstable interface in two and three-dimensional inviscid flow, and was able to determine more accurately the flux of the interface at the cell boundary. The interface was reconstructed by a sloped straight-line segment in a cell rather than by a vertical or horizontal line. The orientation of the segment could be calculated from the known volume fraction in eight neighbours. Several material interfaces could be delineated

in one cell. Puckett (1991) improved the accuracy of Youngs' method, but without reducing its complexity in cylindrical coordinates. In order to avoid this complexity, we have modified the original VOF method, improving the accuracy while maintaining the simplicity of the original formulation even for three-dimensional surfaces. The modified VOF method consists of three steps: (i) Reconstruction of the interface based on the unit normal of the interface; (ii) advection of the interface with the donor-acceptor scheme based on the orientation of the reconstructed interface – an upwinding scheme is implemented when flux parallel to the interface is considered, whereas a downwinding formulation is used when flux normal to the interface is being calculated; (iii) book keeping to restrict the F function to lie between 0 and 1.

The discretization of the integral form of (7) for an incompressible fluid leads to

$$\frac{F_{i,j,k}^{n+1} - F_{i,j,k}^n}{\Delta t} \Delta V_{i,j,k} = - [(u_r FA)_e - (u_r FA)_w + (u_\theta FA)_n \\ - (u_\theta FA)_s + (u_z FA)_t - (u_z FA)_b]. \quad (38)$$

If an upwind scheme is used in all cases, the interface may undergo smearing and lose definition to some extent. In order to avoid this problem in the VOF algorithm used in this work, the differencing scheme chosen for the convection terms is based on the orientation of the interface. It is known (Hirt & Nichols 1981) that a downwind scheme more successfully maintains the sharpness of an interface, especially for a surface which is perpendicular to the flow; on the other hand, such a scheme is numerically unstable due to the introduction of a negative diffusion coefficient. This instability can be bounded by the addition of certain constraints to obtain a realistic solution. Details of the implementation of upwind/downwind schemes in the donor-acceptor algorithm may be found in Hirt & Nichols (1981).

In the original VOF method, the orientation of the interface, as well as whether upwinding or downwinding was to be used, were determined by an approximated distance function. The reconstructed interface could only be either parallel or perpendicular to the interface. This approach, while being reasonably accurate and easy to implement for a two-dimensional flow in Cartesian coordinates, becomes extremely cumbersome in three dimensions and particularly so in cylindrical coordinates in view of the radius dependence of the control volumes.

In order to overcome this problem, the unit normal to the interface is used in the present work for determining the orientation of the surface, in which the interface can be adjusted based on the flow field as illustrated in figure 2. For example, the interface in figure 2(a) can only be constructed to be perpendicular to the r -direction in the original VOF method (figure 2b) even when the flow is mainly in the z -direction; surface smearing is thus unavoidable. In contrast, the use of a unit normal (figure 2c) allows this surface to be constructed parallel to the r -direction. This allows a downwind scheme to be used when the fluxes at the n and s faces of the cell are calculated, with the other faces being treated in the same manner.

To demonstrate this method, the axisymmetric rise of a sphere with a constant velocity, $\mathbf{v}\{r, \theta, z\} = \{0, 0, 0.5\}$ in a cylinder was simulated as a test problem. The mesh size was 80×38 and the time step was 0.01. In the results shown in figure 3, setting n_r and $n_z = 0$ implies that a pure downwind scheme is adopted, while n_r and $n_z = 1$ indicates that a pure upwind scheme is used. By studying the effect on interface reconstruction of adjusting the criteria for defining a parallel or perpendicular surface, it can be seen that a pure upwind scheme results in severe smearing (figure 3b); conversely, the excessively non-diffusive pure downwind scheme is observed to result

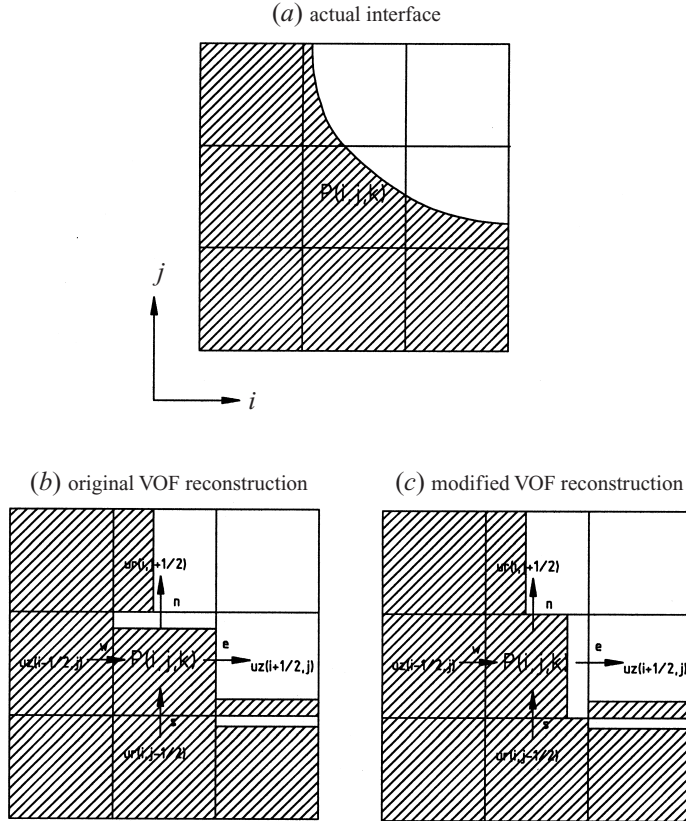


FIGURE 2. Different reconstructions realized by the original and modified (present work) VOF methods.

in considerable flotsam (figure 3c). Reasonable results are obtained when a combined upwind/downwind scheme is used and the switch from upwind to downwind schemes is effected when n_x or n_z exceed a value in the range of 0.2 to 0.4 (figure 3d); in this study a value of 0.4 was used to control the switch. This method reconstructs an interface which has an angle smaller than 30° to the z -direction as a surface parallel to the z -direction, and allows a downwind scheme to be used. This flexible definition of a parallel or perpendicular surface depending on the flow field appears to be successful in reducing numerical diffusion. Another advantage of this proposed modification is that the accurately computed unit normal is very easy to extend to any coordinate system.

The combination of upwind and downwind schemes used in this work cannot entirely prevent the smearing of the interface, especially when it is nearly parallel to the interface and the upwind scheme is still in use. This numerical diffusion is strongly dependent on the mesh size, as may be seen in figure 4 presented in § 4. It should be noted that the interface must be smeared across at least one mesh point since F changes from zero to unity across, at the very minimum, one mesh interval. Finer meshes would obviously reduce the smearing but would render the solution more computationally expensive.

3.5. The solution procedure

At each time step, the velocity \mathbf{U}^* is found from (32) using the pressure available from the previous time step. The pressure correction is solved using (33). The velocity and

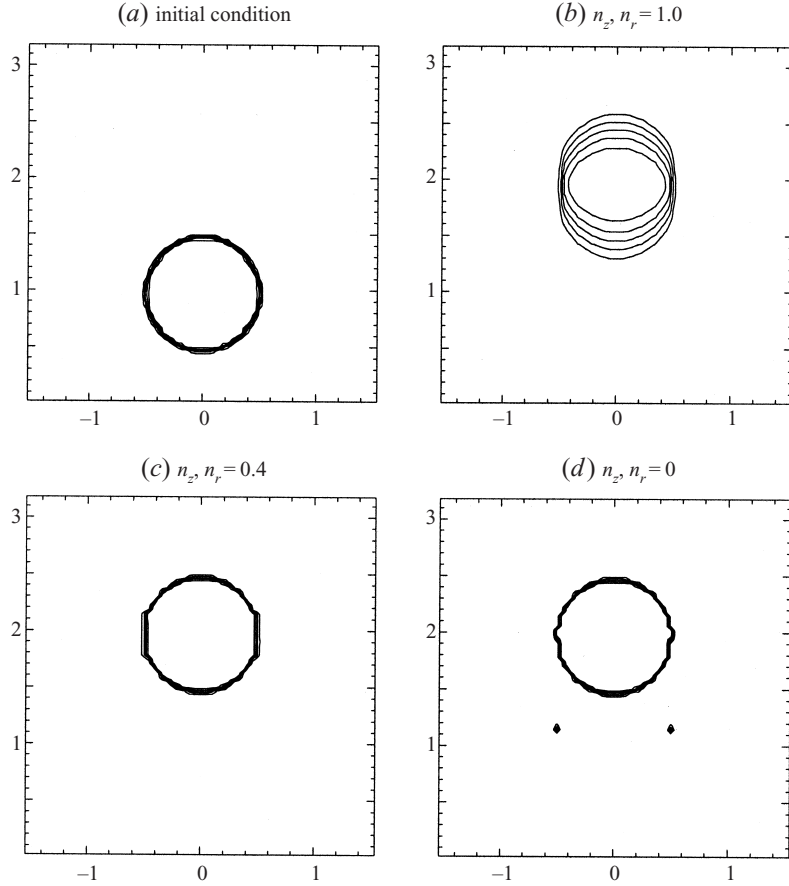


FIGURE 3. Translation of a sphere with different combinations of upwind and downwind schemes ($\Delta z = \Delta r = 0.04$, $\Delta\tau = 0.01$, after 500 iterations).

pressure are updated by solving (35) and (36), and (2) is checked to verify conservation of mass; the iteration is repeated until the conservation condition, $|\nabla \cdot \mathbf{U}| \leq 10^{-4}$ is achieved. Equation (7) is then solved to obtain the new location of the interface, and the surface tension force is calculated. Thereafter, the calculation proceeds to the next time step. If a sufficiently small time step (Courant number ≤ 1) is used, a mass conservation is satisfied in approximately 10 inner iterations. This procedure also allows an implicit implementation of a surface tension force.

4. Results and discussion

The effect of varying the mesh size on the accuracy of the solution was investigated by studying the axisymmetric rise of an isolated, initially spherical bubble in a liquid with the following parameters: $Bo = 50$, $Re = 100$, $\rho_f/\rho_g = 80$ and $\mu_f/\mu_g = 80$. The results were generated on three sets of grids ($z \times r$) of 54×17 , 108×34 and 216×68 with $\Delta\tau = 0.004$, 0.001 and 0.00025 , respectively. The CPU time per cell per iteration with the three mesh sizes was 1.22 , 1.58 and 2.52 ms respectively on a DEC Alpha 800 workstation. Results for the mesh sensitivity of the calculated shape of the bubble at $\tau = 2.0$ are shown in figure 4. Multiple contours for $0 \leq F \leq 1$ are included. (In

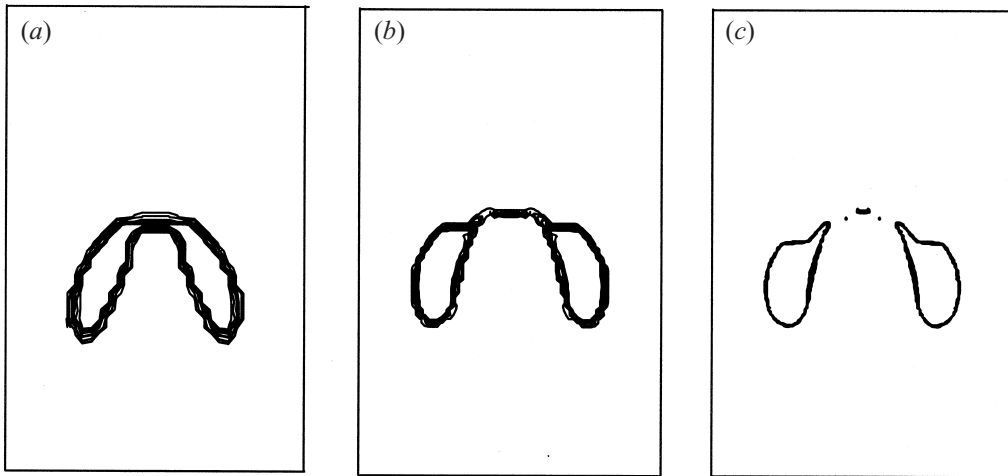


FIGURE 4. Effect of mesh size on the solution: (a) 54×17 , (b) 108×34 , and (c) 216×68
($Bo = 50$, $Re = 100$, $\rho_f/\rho_g = 80$, $\mu_f/\mu_g = 80$; $\tau = 2.5$).

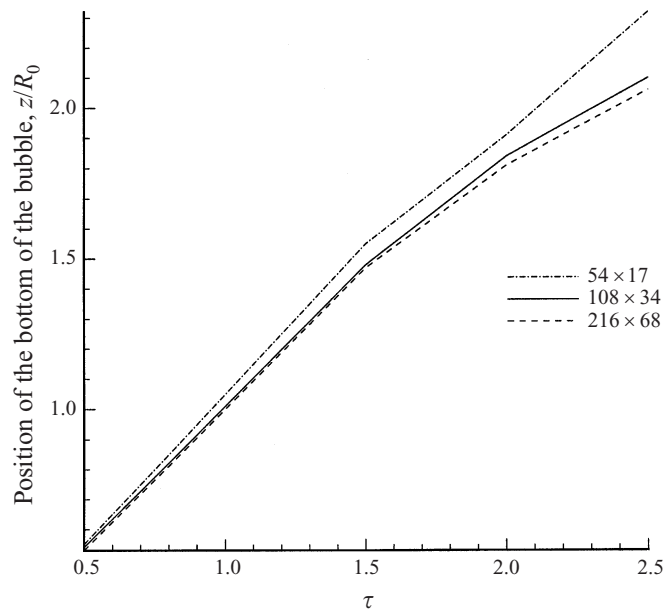


FIGURE 5. Effect of grid size on bubble rise velocity in a closed cylinder
($Bo = 50$, $Re = 100$, $\rho_f/\rho_g = 80$, $\mu_f/\mu_g = 80$).

the remaining figures in this paper, the contours representing the bubble are those for $F = 0.5$.) Figure 5 shows the effect of mesh size on the calculated bubble position as a function of time (bubble rise velocity). The intermediate grid size, 108×34 , is shown to yield solutions of sufficient accuracy (with respect to the trade-off between computational cost and identification of the features being studied), and is chosen for the results presented in this paper. For the full three-dimensional calculation, a mesh size of $78 \times 23 \times 12(z \times r \times \theta)$ was used. While a finer grid in the circumferential direction would be preferable to properly identify the finer three-dimensional features

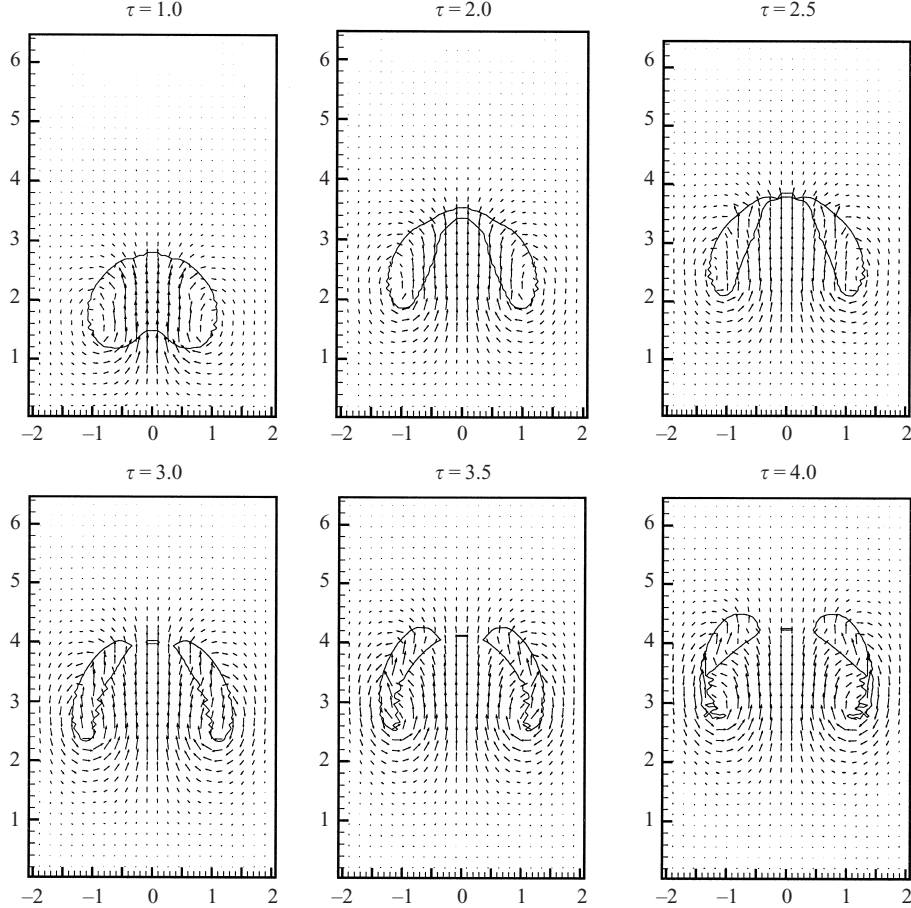


FIGURE 6. Velocity vectors for a gas bubble rising in a viscous liquid ($Bo = 50$, $Re = 100$, $\rho_f/\rho_g = 1000$, $\mu_f/\mu_g = 80$); the solid line indicates the shape of the bubble with the $F = 0.5$ contour.

of the bubble rise and distortion, the essential elements of the present computations are illustrated adequately with this mesh.

4.1. The rise of a gas bubble in a liquid with a large density ratio

The general features of the rise of a gas bubble in a liquid, and its distortion at a high Bond number and Reynolds number are illustrated in figure 6. All results in this paper were computed for a cylinder-diameter to initial bubble-diameter ratio of 2.07. A rather crinkly surface is noticed in the figure when a vortex forms behind the toroidal bubble. This surface could be better resolved by refining the grid (as demonstrated in figure 4), but at added computational expense. The grid used in figure 6 is considered adequate to resolve the features of the flow.

When the bubble begins to rise owing to buoyancy, the pressure gradient at the lower surface of the bubble is higher than that at the top surface, and the vortex sheet which develops at the surface has a sense of rotation which induces the motion of a jet of water what pushes into the bubble from below, as may be seen in the figure at $\tau = 1.0$ and 2.0 . At this stage, the jet does not yet affect the liquid above the bubble. The velocity of the upper surface relative to the rest of the bubble decreases with increasing time, so that the bubble takes the form of a shell. As time progresses the

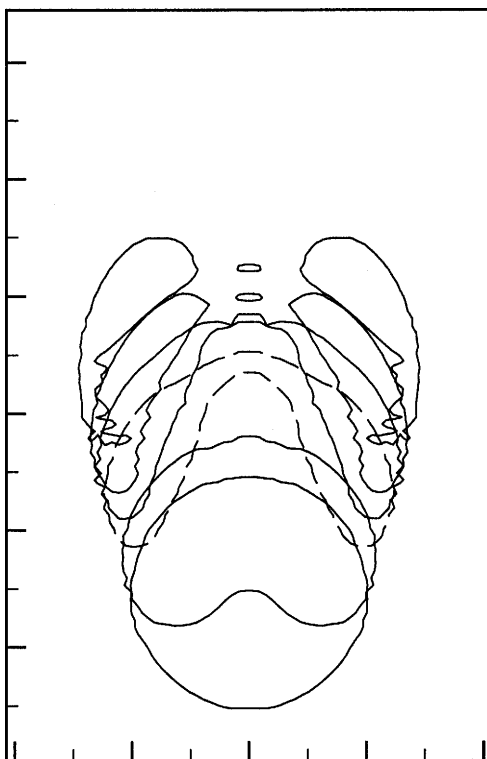


FIGURE 7. Shape evolution of an air bubble rising in a viscous liquid for the same parameters as figure 6.

water jet further penetrates the bubble, which results in the lower surface approaching the bubble cap. Eventually the impact of the jet results in the lower surface piercing the top surface of the bubble ($\tau = 2.5$); in the process, a thin air pocket is carried into the liquid above the bubble which forms a small new bubble at the centre, followed below by an annular toroidal bubble ($\tau = 3.0$). The vorticity in the bubble surface is transferred to circulation about this annular toroidal bubble ($\tau = 3.0, 3.5$) and ultimately, this toroid breaks up into a ring of small bubbles in order to preserve the circulation. The shape development of the bubble is shown as a set of superimposed calculations in figure 7.

The features of three-dimensional bubbles reported from the experiments of Walters & Davidson (1963) included the deformation of the lower surface of the bubble by a jet of liquid forming a so-called liquid tongue, “the piercing of the top surface and the resultant formation of a toroidal bubble with a very small bubble in the centre”, and an increase in the diameter of the toroidal bubble as it rises further. The inner and outer radii of the toroid increase as it rises, and the toroidal bubble ‘expands’ slightly. This may be explained in terms of the requirement of a stabilized circulation (Pedley 1968; Lundgren & Mansour 1991). During the rise of their two-dimensional bubbles, Walters & Davidson also observed the detachment of two small bubbles at the lower extremities of the main bubble, each of the two detached bubbles being at the centre of a vortex. Even the predicted formation of a small bubble at the centre of the toroid formed (shown in figure 6) is in accordance with the findings of Oguz & Prosperetti (1989) for the contact between free surfaces. They reported that owing

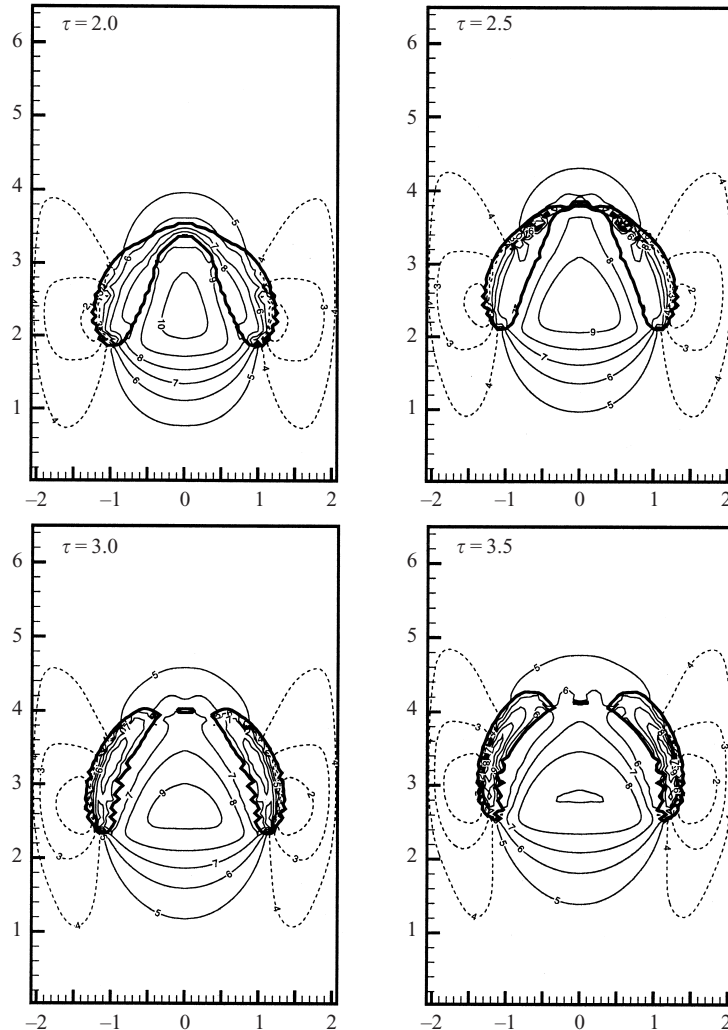


FIGURE 8. Vertical velocity contours for a gas bubble rising in a viscous liquid for the same parameters as figure 6; the thick solid line indicates the shape of the bubble with the $F = 0.5$ contour; the dotted lines indicate negative values of velocity. Contour levels 1 to 10 have the values $-0.9, -0.622, -0.343, -0.065, 0.214, 0.492, 0.771, 1.049, 1.33$ and 1.61 , respectively.

to surface tension, the touching of two free surfaces leads to the liquid contacting at a number of points away from the initial contact element so that the gas entrapped between these multiple contact points forms a series of bubbles. As seen later in the present work (figure 10c), as the surface tension is decreased the jet tends to penetrate the upper surface at a single point so that no small bubbles are formed at the centre. These observations suggest that an increase in surface tension leads to a wave-like disturbance when the contact of upper and lower surfaces of the bubble occurs.

The development of the liquid jet leading to the formation of the toroidal bubble is further shown in the velocity contour plots of figure 8. The liquid jet is seen to push the lower surface of the bubble, becoming increasingly broad after piercing the top surface. The rise velocities computed at the highest point of the upper and lower surfaces of the bubble are shown in figure 9; the velocity of the lower surface of

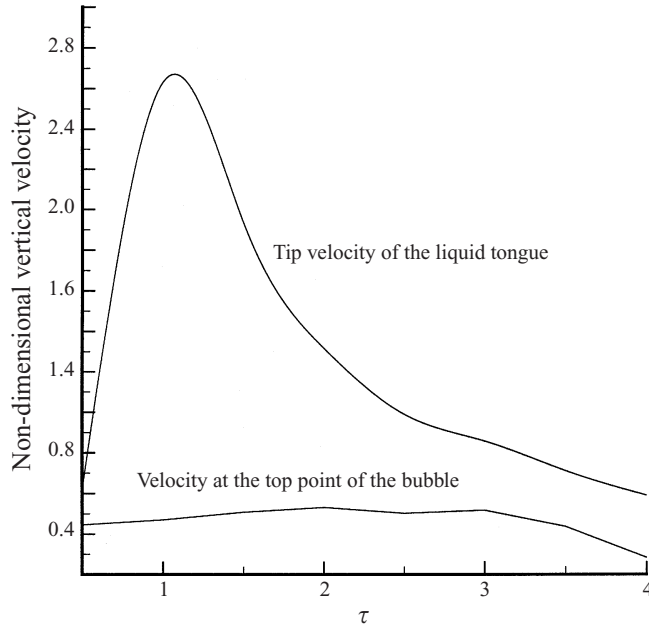


FIGURE 9. Vertical velocities at the highest point on the lower and upper surfaces of the bubble for the same parameters as figure 6.

the bubble represents the liquid jet characteristics. It may be seen that the liquid jet accelerates first. As the liquid jet approaches the upper surface it decelerates due to the increase in the surface-tension force caused by the increased curvature. This deceleration is aided by the increase in surface area which in turn increases the viscous force opposing the jet motion. The velocity in the liquid above the bubble is nearly constant. After the contact of the liquid tongue with the top surface of the bubble, the liquid in the jet flows through the resulting torus with a velocity which decreases with time. This is accord with the principle that surface tension tries to maintain a shape to minimize the surface energy and acts as a resistive force opposing the motion of the liquid tongue.

4.2. The role of surface tension in the formation of a toroidal bubble

The effect of surface tension on the development of the bubble is illustrated in figure 10 by varying the Bond number whilst keeping the remaining parameters constant. At the lowest Bond number, the water jet formed below the bubble deforms the lower surface of the bubble and a shell forms (figure 10a, $\tau = 1.5, 2.0$). Owing to the high surface tension, the liquid tongue below the bubble is unable to penetrate the upper surface, and an elliptical bubble forms. As time progresses, a vortex ring forms below the bubble ($\tau = 4.0$). A decrease in surface tension (i.e. a higher Bond number) results in a greater distortion of the lower surface of the bubble so that a mushroom-shaped bubble forms first; in this case, the impact of the liquid tongue has occurred by $\tau = 3.0$ as in figure 10(b). With a further reduction in surface tension, the piercing of the top surface occurs earlier in time, as may be deduced from figure 10(c). The vertical velocity profiles along the diameter of the cylinder are plotted in figure 11 for the plane $z = 2.2$ near the lowest point of the bubble, in order to observe the penetration strength of the liquid jet. From figure 11 it can be seen that the jet velocities for

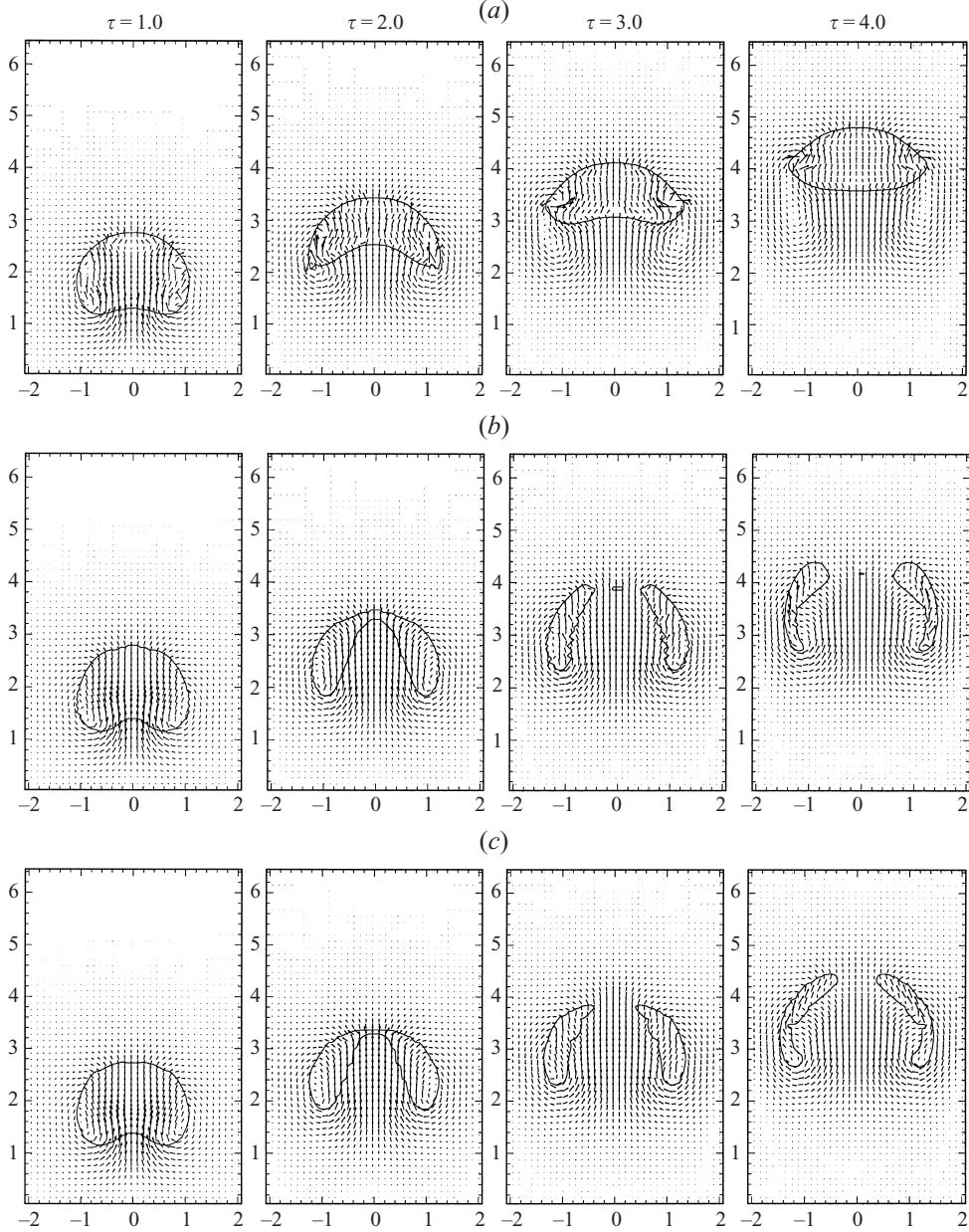


FIGURE 10. The effect of surface tension on bubble rise ($Re = 100$, $\rho_f/\rho_g = 80$, $\mu_f/\mu_g = 80$):
 (a) $Bo = 5$, (b) $Bo = 50$ and (c) $Bo = 500$.

$Bo = 50$ and 500 are quite similar, whereas a lower Bond number of 5 results in a significantly lower vertical velocity with a flatter profile. These observations are consistent with the claim of Lundgren & Mansour (1991) and Marten *et al.* (1996) that small toroidal bubbles cannot be formed via a simple gravitational mechanism.

It may be noted from figures 10(b) and 10(c) that a longer toroid is obtained when the surface tension is lower; a slower rise of such a toroid may be expected due to the increased shear stress for this shape. By the same reasoning, an elliptical bubble

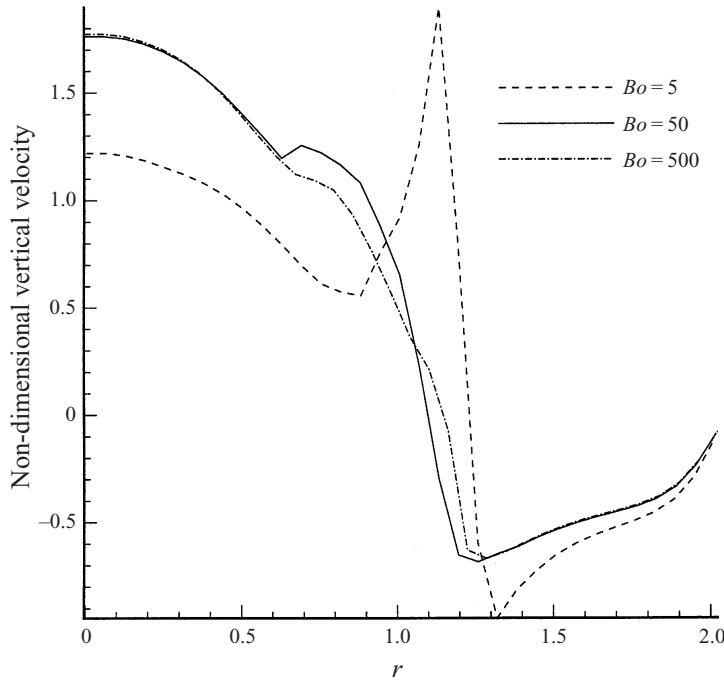


FIGURE 11. Vertical velocity profiles in the radial direction at $z = 2.2$ and $\tau = 2.0$ ($Re = 100$, $\rho_f/\rho_g = 80$, $\mu_f/\mu_g = 80$) for three different Bond numbers of 5, 50 and 500.

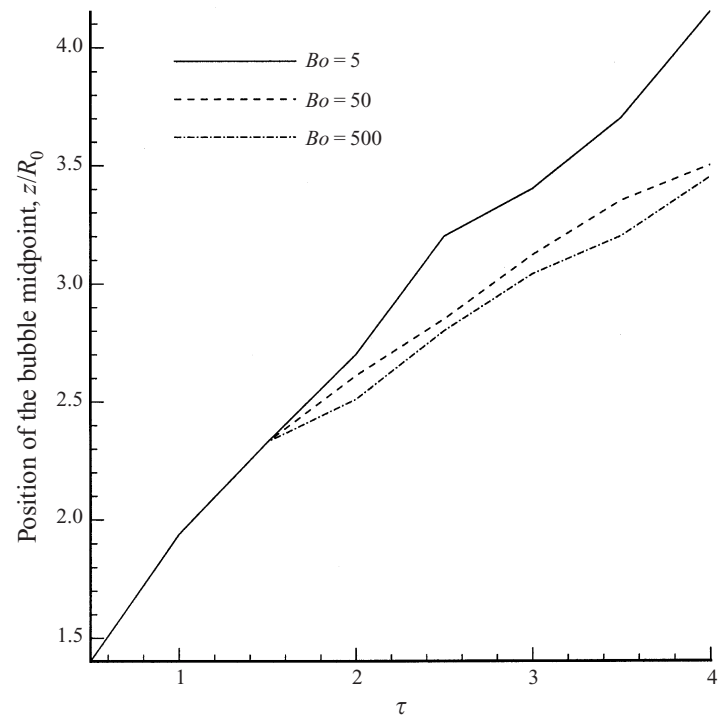


FIGURE 12. Position of the centre of the bubble as a function of time for different Bond numbers:
 $Re = 100$, $\rho_f/\rho_g = 80$, $\mu_f/\mu_g = 80$.

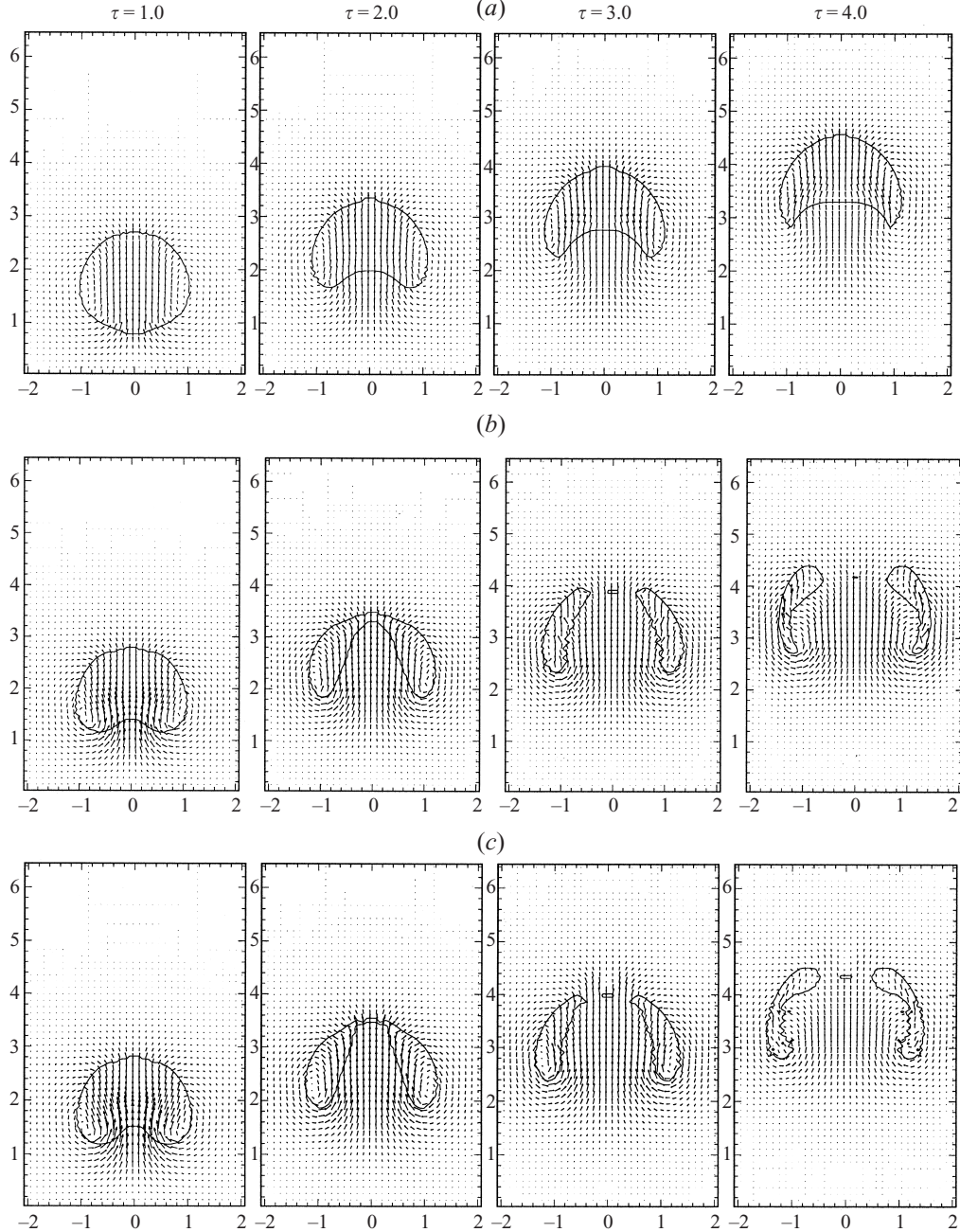


FIGURE 13. Influence of Reynolds number on the motion of a bubble rising along the axis of the cylinder: $Bo = 50$, $\rho_f/\rho_g = 80$. The Reynolds numbers are (a) 10, (b) 50, and (c) 500.

would be expected to achieve the highest rise velocity because the circulation around the toroidal bubble impedes its rise. This is demonstrated in figure 12, where the bubble position history is shown for the midpoint between the lowest and topmost positions of the elliptical or toroidal bubble. The ellipse is seen to travel faster than the toroid. Also, the longer toroid ($Bo = 500$) has the lowest rise velocity. At $\tau = 4.0$,

the rise velocity is 16% lower for a Bond number of 50 relative to that for $Bo = 5$. Comparing the two toroidal bubbles, however, the decrease in rise velocity for an increase in Bond number from 50 to 500 was only 2.8%. The primary effect of a reduction in surface tension (increase in Bond number) on the bubble dynamics is thus manifested as a change in shape of the bubble from elliptical to toroidal.

4.3. The role of fluid viscosity in the formation of a toroidal bubble

The effect of Reynolds number on the motion of the bubble is illustrated in figure 13. For a very low Reynolds number (large viscosity), the liquid jet below the bubble is very weak and the bubble rises as a cap, as may be seen in figure 13(a). The velocity on the lower surface of the bubble increases with an increase in Reynolds number and eventually, when the Reynolds number reaches 50, the jet pierces the top surface and the bubble forms a toroid as shown in figure 13(b). For a further increase in Reynolds number to 500, the formation of the toroid occurs earlier in time and the toroid spreads outward to a greater extent, as shown in figure 13(c).

A more detailed description of the flow field is presented in figure 14, where the vertical velocity contours at four different times for each of the Reynolds numbers are shown. In the region below the bubble, the velocity contours vary significantly as the Reynolds number is varied. A higher Reynolds number results in a stronger jet in the region below the bubble. The jet also penetrates the relatively quiescent liquid above the bubble with a higher velocity at the higher Reynolds numbers, as evidenced by the more sharply varying and larger values of the contours in the region of the torus in figures 14(b) and 14(c) at $\tau = 3.0$. At the lower Reynolds numbers, the higher viscosity increases the form drag and reduces the liquid jet velocity; a broader, more diffuse velocity distribution results, which is unable to penetrate the upper surface, thus causing the bubble to assume an elliptic-cap shape.

The predicted shape development using the modified VOF method of this work is in good agreement with the experiments of Bhaga & Weber (1981), as seen in figure 15. The simulation in figure 15a is performed at a Morton number ($M = Bo^3/Re^4$) of 1.31 and a Bond number of 29, to match the experimental conditions of figure 3e from Bhaga & Weber (the Bond number of 116 reported for the experiments was based on the bubble diameter instead of bubble radius used as the characteristic length in the present work). Bhaga & Weber presented the actual rise velocity U in terms of a Reynolds number based on a volume-equivalent diameter ($R = \rho d_o U / \mu$), which is comparable to $ReU/(gR_0)^{1/2}$ in the present computations. The rise velocity is computed with reference to the top of the bubble. The experimental Reynolds number (based on bubble radius) was 10.2 while the predictions yield 10.01. The oblate ellipsoidal-cap shape obtained in both the results is characterized by an aspect ratio (minor-to-major axis ratio of the ellipse) of 0.76 for the experiment and 0.83 for the prediction. Also, the included angle at the centre of the ellipse between the vertical and the bottom-most ray is 99° in the experiment, and 104° in the prediction. Given the somewhat uncertain initial conditions in the experiment, the agreement between these results may be considered very satisfactory. It should be noted that the numerical simulation in figure 15(a) shows a cross-section through the midplane of the bubble. Since the photograph shows a frontal view, the concave shape of the bottom of the bubble seen in the numerical simulation is obscured in the photograph. However, the visual observation of ‘a significant indentation or dimple’ at the base, which is a manifestation of the closed toroidal wake accompanying the bubble, is reported in Bhaga & Weber (1981). Another simulation at a higher Morton number of 266 is shown in figure 15(b), which matches the experimental conditions of figure

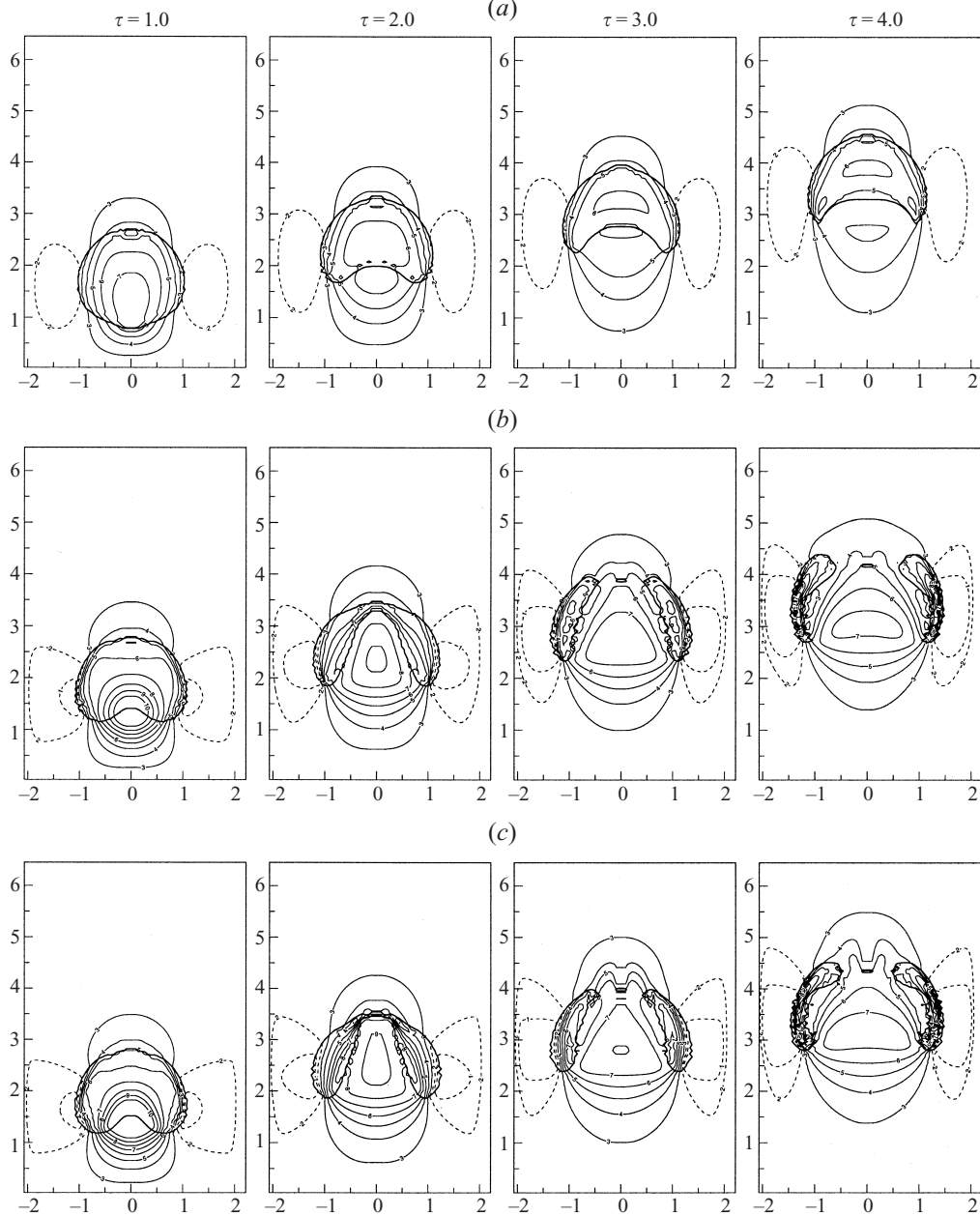


FIGURE 14. Vertical velocity contours for different Reynolds numbers ($Bo = 50$, $\rho_f/\rho_g = 80$ and $\mu_f/\mu_g = 80$): (a) $Re = 10$ (b) $Re = 100$ and (c) $Re = 500$. Contour levels 1 to 10 have the values $-0.411, -0.143, 0.125, 0.393, 0.661, 0.928, 1.2, 1.46$ and 1.73 , respectively.

3(b) from Bhaga & Weber. The experimental values in this case for Reynolds number, bubble aspect ratio and included angle were 1.79° , 0.86° and 120.07° , respectively. The corresponding predicted values of 1.70° , 0.95° and 126.25° again agree well with experiment. In addition to these comparisons with experiment, it was shown in the experiments of Walters & Davidson (1963) that for inviscid fluids, the bubble breaks up into a toroid – this is consistent with the predicted results.

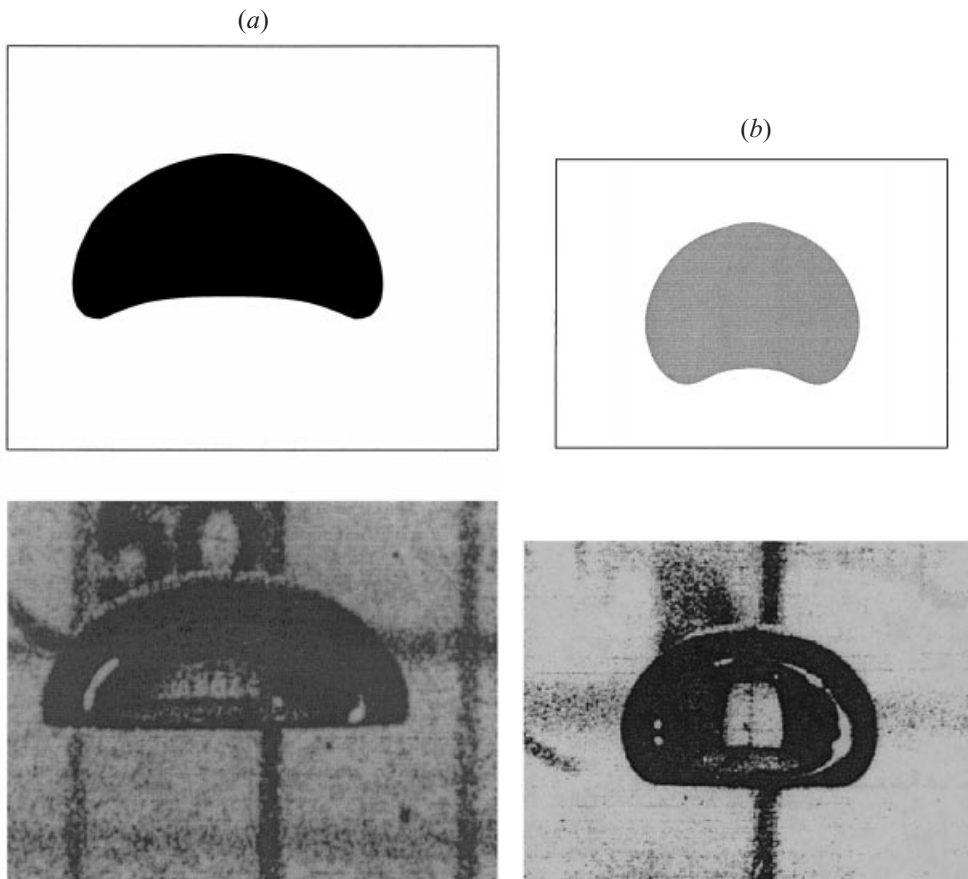


FIGURE 15. Comparison of predicted results with the experiments of Bhaga & Weber (1981): (a) $Bo = 29$, Morton number = 1.31; (b) $Bo = 29$, Morton number = 266. (Photographs from figures 3e and 3b of that paper used with permission.)

Figure 16 shows the position of the middle of the bubble as a function of time for the three Reynolds numbers modelled. For a given shape, the bubbles are seen to rise faster at the higher Reynolds number. This can be readily explained since a decrease in the viscosity leads to a decrease in the resistance to bubble rise for any shape. The elliptic-cap bubble formed at $Re = 10$ does not form a toroid and rises at a steady velocity, as indicated by the nearly constant slope in the figure. Once the bubble can become toroidal in shape, as at $Re = 100$ and 500, the rise velocities start to drop (seen as a change in slope in the figure), eventually falling below the velocity of the elliptic bubble, as the result of an exchange of momentum when the impact of the liquid jet occurs and transient circulation is set up around the toroidal bubble. Further, the formation of a toroidal bubble results in an increase in the area of the shear layer around the bubble, accompanied by an expected decrease in velocity around the toroid.

4.4. The effect of density and viscosity ratios on the bubble rise

An increase in the density ratio (ρ_f/ρ_g) between the two fluids leads to an increase in the buoyancy force, resulting in a higher rise velocity for the bubble. Three density ratios of 1000, 80 and 5 were investigated for their effect on bubble motion, and the results are presented in figure 17. For the higher density ratios, $\rho_f/\rho_g = 1000$ and 80,

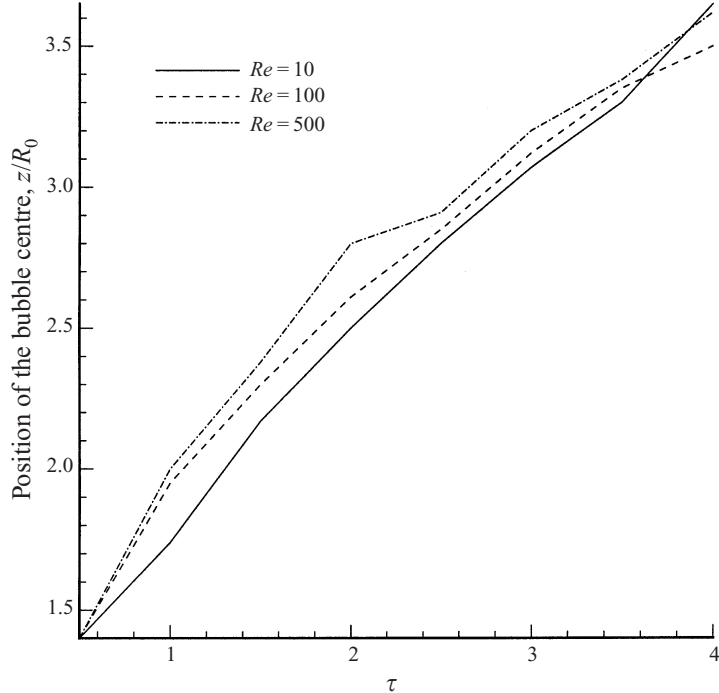


FIGURE 16. Position of the centre of the bubble as a function of time for different Reynolds numbers $Bo = 50$, $\rho_f/\rho_g = 80$ and $\mu_f/\mu_g = 80$.

the development of bubble shape with time is similar (figures 17a, 17b). However, it can be seen that a significant delay in the formation of the toroid (the piercing is not quite complete even by $\tau = 4$ in figure 17c) results from a very low buoyancy force (i.e. small density ratio, $\rho_f/\rho_g = 5$).

A higher density ratio results in a faster rise of the bubble in all cases, up to the time that the bubble has not undergone a significant shape change, such as the formation of a toroid; this is true of the period before $\tau = 2.5$ in figure 18. After the formation of a toroid at $\tau = 2.5$, the rise velocities are reduced for $\rho_f/\rho_g = 1000$ and 80 due to the vortex formed around the toroid. In contrast, the skirted bubble (not pierced, and hence not yet a toroid) formed at the lowest density ratio continues to travel at a constant velocity and gradually catches up with the toroidal bubbles ($\rho_f/\rho_g = 1000$ and 80) at $\tau = 3.5$. For a given shape, however, a higher density ratio results in a faster rise velocity. This observation reveals the contribution of gravitational forces to the formation of a toroidal bubble.

A change in the viscosity ratio was found not to alter the shape histories significantly in the range investigated ($40 \leq \mu_f/\mu_g \leq 80$).

The role of surface tension and viscosity, the primary determinants of the shape of the bubble as it rises, are summarized in a map plotting Bond number against Reynolds number in figure 19.

To demonstrate the capability of the algorithm, three-dimensional simulations of the motion of a bubble were performed, for which the results are shown in figures 20(a) and 20(b). Two sets of parameters were used in the three-dimensional simulations: $Re = 10$, $Bo = 5$, $\rho_f/\rho_g = 40$, $\mu_f/\mu_g = 40$; and $Re = 100$, $Bo = 50$, $\rho_f/\rho_g = 80$, $\mu_f/\mu_g = 80$. Because the flow is axisymmetric, a coarse mesh in the θ -direction

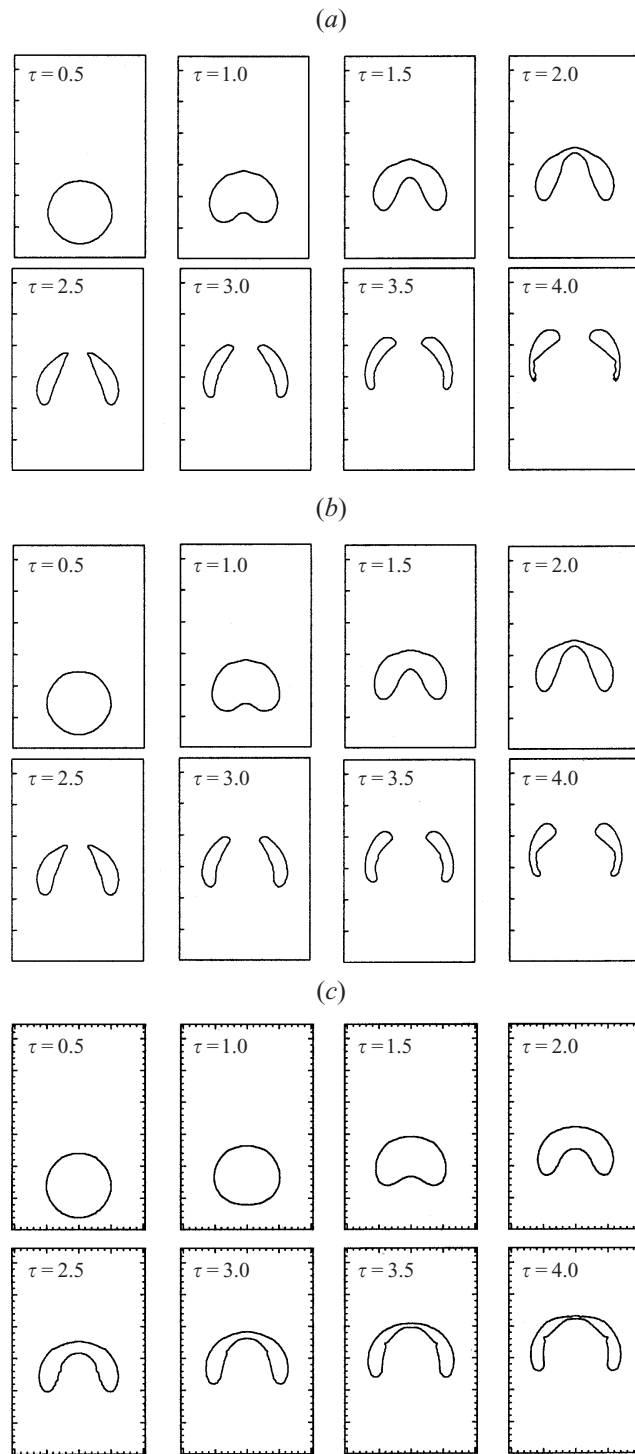


FIGURE 17. The effect of density ratio on the motion of a bubble rising along the axis of a cylinder; $Bo = 50$, $Re = 100$, $\mu_f/\mu_g = 80$; the density ratios are (a) 1000, (b) 80, and (c) 5.

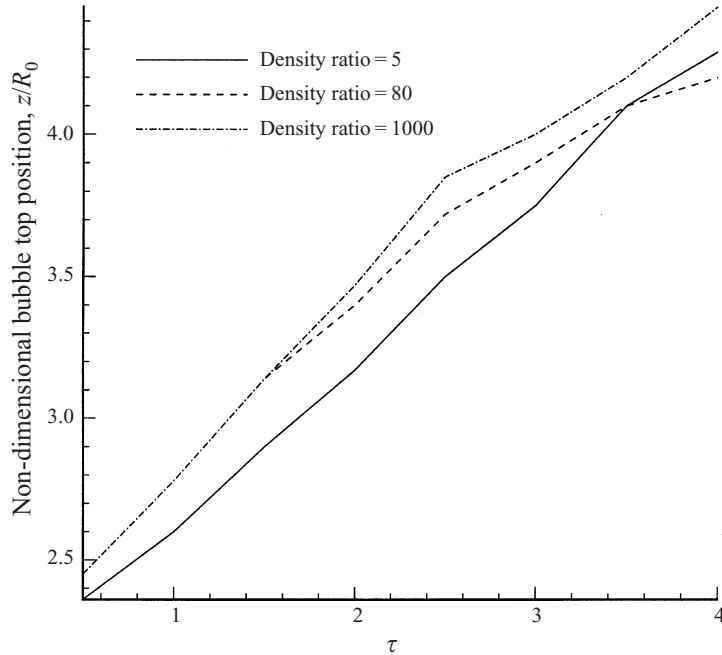


FIGURE 18. Position of the top of the bubble as a function of time for different density ratios and same parameters as figure 17.

was sufficient, and a $78 \times 23 \times 12$ mesh is adopted. It may be seen that the shape development of the bubble shown in these figures is similar to those depicted in figures 13(a) and 10(b) for the corresponding two-dimensional simulations. The deformation of a bubble from a sphere to an elliptic cap and the formation of a toroidal bubble can be clearly seen in the three-dimensional simulations. As in the two-dimensional simulations, these figures show that at low Bond and Reynolds numbers (high surface tension and viscosity), the bubble does not break up.

4.5. The development of a wake beneath the bubble

During its rise and development, if a bubble does not break into a toroidal ring, a wake may form at its trailing end depending on the Bond number and Reynolds number. As the bubble rises with a continuous increase in its surface curvature, an accumulation of vorticity at its rear may result in wake formation after the bubble reaches a nearly steady shape. The conditions (Bo and Re) under which a wake forms, the length and width of the wake, and its relationship to the aspect ratio of the bubble are discussed in this section. According to Bhaga & Weber (1981), for high-Morton-number fluids, $M \geq 4 \times 10^{-3}$, the wake behind a rising bubble becomes unstable when the rise velocity based Reynolds number (R , defined earlier) is greater than 110. At these Reynolds numbers, Hartunian & Sears (1957) and Wegener & Parlange (1973) experimentally determined that the travel path of small bubbles ($Bo = O(1)$) becomes oscillatory even for low Morton numbers.

For bigger bubbles ($Bo > 15$) with high Reynolds number and a spherical-cap shape, an unstable or turbulent wake was observed. In the light of these experimental observations, the simulations for deforming (but not toroidal) bubbles in the present work were limited to the parameter ranges, $3 \leq Bo \leq 50$ and $5 \leq Re \leq 250$; this ensures that the bubble rise is stable and axisymmetric.

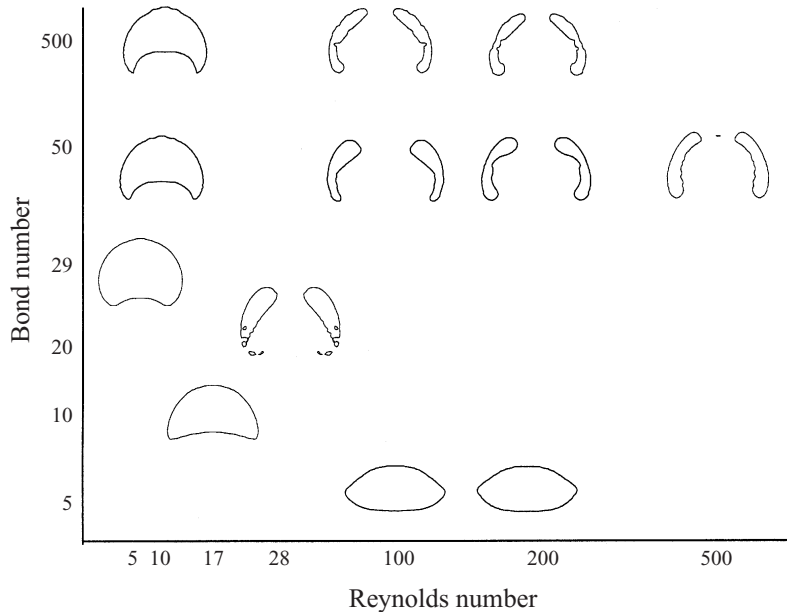


FIGURE 19. Map of bubble shape as a function of Reynolds and Bond numbers ($\rho_f/\rho_g = 80$ and $\mu_f/\mu_g = 80$).

The influence of Bond number on the shape development of the bubble, and hence, on the wake formation is illustrated in figure 21. At a Bond number of 1.5, with $Re = 10$ ($M = 3 \times 10^{-4}$), $\rho_f/\rho_g = 80$, and $\mu_f/\mu_g = 80$, the shape of the bubble gradually changes from spherical to oblate ellipsoidal during its rise, and vorticity is gradually accumulated around the bubble with an increase in surface curvature along its sides. When the bubble reaches the nearly steady shape of an oblate ellipsoid with aspect ratio ($2b/h$, where $2b$ is the maximum bubble diameter and h is the distance from the front stagnation point to the rear stagnation point of the bubble) equal to 1.67, vorticity production near the bubble is just sufficient to support the reversal of flow in a very small region behind the bubble, and the hint of a wake is detected (figure 21a). It may be noted that only the velocity field in the liquid is plotted in the figures for clarity and that this velocity is calculated relative to the front stagnation point of the bubble. The results are shown at $\tau = 3.5$ by which time the bubble has reached a nearly unchanging shape.

For a small increase in Bo to 3 with the rest of the parameters held constant, the bubble takes an ellipsoidal-cap shape with an aspect ratio of 1.82 and small wake is visible (figure 21b). Increasing Bo from 3 to 5 causes the bubble to deform further, with its aspect ratio increasing to 1.97. The wake is significantly stronger in this case (figure 21c). Finally, for a considerably larger Bo of 30, a strong wake is established behind the shell-like bubble which now has an aspect ratio of 2.63 (figure 21d). The length of the wake is seen from figure 21 to increase with an increase in Bo , even though the rise velocity simultaneously decreases as discussed in a previous section. The changes in the bubble aspect ratio and in the length of the wake (L/b) with increasing Bond number are shown in figure 22; as in past studies, the wake is considered to extend in length from the bottom of the bubble to the point at which the vertical velocity takes a value of zero.

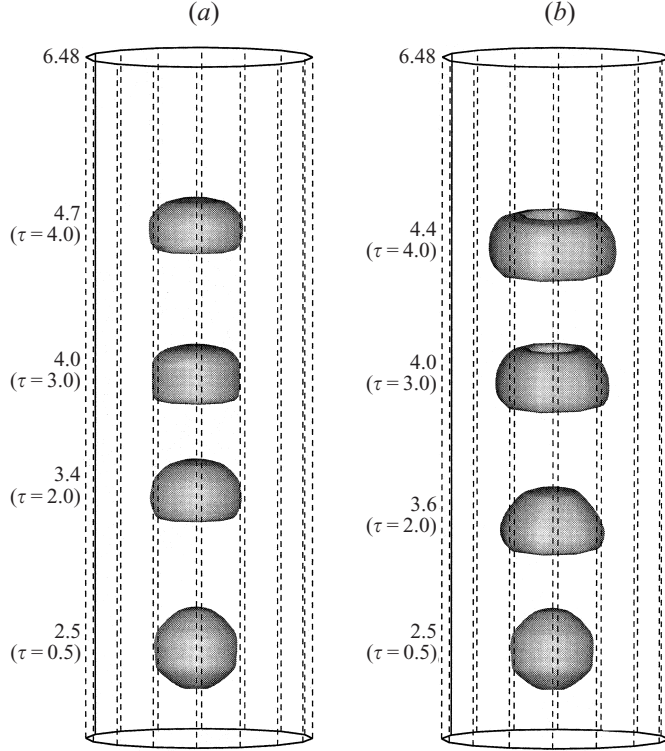


FIGURE 20. Three-dimensional simulations of the growth of a bubble: (a) $Bo = 5$, $Re = 10$, $\rho_f/\rho_g = 40$ and $\mu_f/\mu_g = 40$ (compare with the two-dimensional simulations in figure 13a); (b) $Bo = 50$, $Re = 100$, $\rho_f/\rho_g = 80$ and $\mu_f/\mu_g = 80$ (compare with the two-dimensional simulations in figure 10b). The z-locations of the top of the bubble are shown on the left.

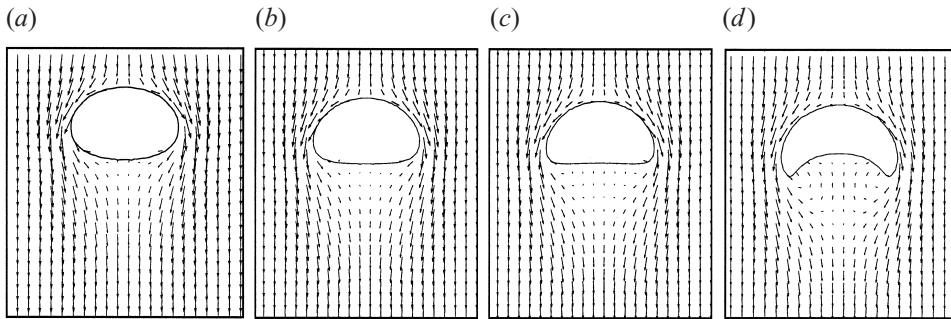


FIGURE 21. Development of a trailing wake as a function of Bond number ($Re = 10$, $\rho_f/\rho_g = 80$ and $\mu_f/\mu_g = 80$). Bond number values (with bubble aspect ratio included in parentheses) are: (a) 1.5(1.67), (b) 3(1.82), (c) 5(1.97), and (d) 30(2.63).

Since the rise velocity of small bubbles is determined mainly by the Reynolds number, its effect on wake formation is investigated further (figure 23), with the Bond number held constant at a small value of 5 so as to maintain the integrity of the bubble i.e. to prevent bubble breakup). The viscosity and density ratios are also held constant at 80 each. At $Re = 5$ (figure 24a), the bubble has deformed into an oblate ellipsoid with an aspect ratio of 1.53. No wake is observed. For a slight increase in

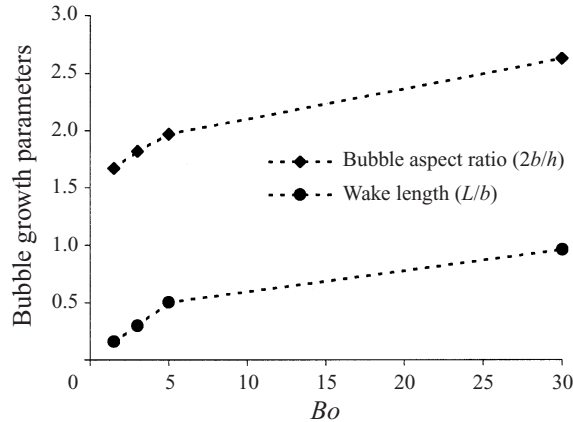


FIGURE 22. Bubble aspect ratio and wake length as a function of Bond number for the cases shown in figure 21.

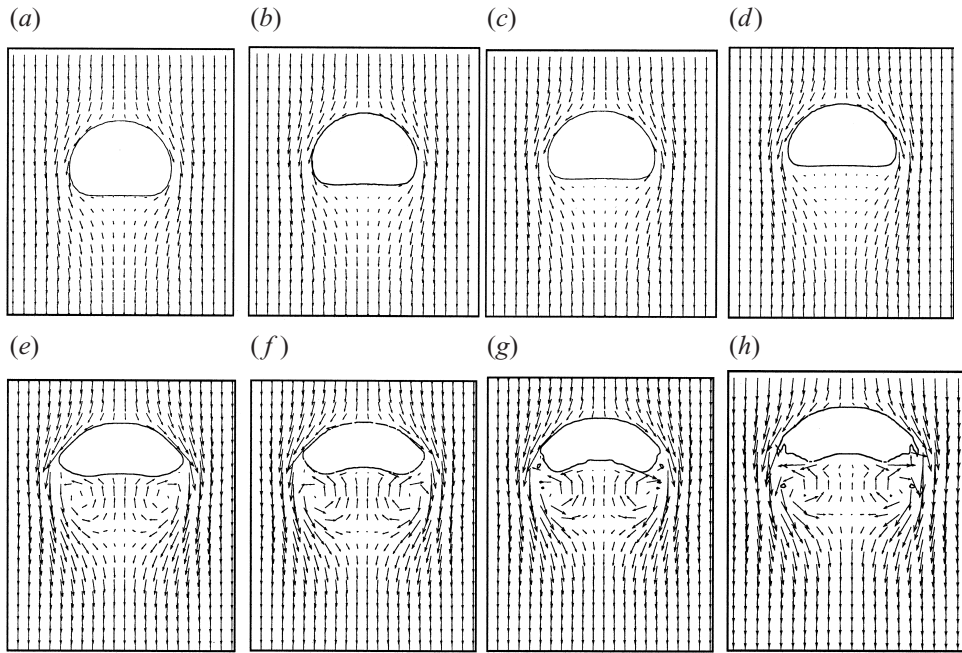


FIGURE 23. Development of a trailing wake as a function of Reynolds number ($Bo = 5$, $\rho_f/\rho_g = 80$ and $\mu_f/\mu_g = 80$). Reynolds number values (with bubble aspect ratio in parentheses) are: (a) 5(1.53), (b) 6(1.67), (c) 7(1.75), (d) 10(1.97), (e) 50(2.73), (f) 100(3.02), (g) 200(3.20), (h) 250(3.31).

Re to 6 (figure 24b), the bubble deforms to an ellipsoidal-cap shape with a larger aspect ratio of 1.67, but still, no wake is observed. A weak wake becomes evident for a further increase in Re to 7 (figure 24c) with the aspect ratio of the ellipsoidal-cap bubble having increased to 1.75. The length of the wake, L/b , is 0.19 in this case. The wake becomes longer ($L/b = 0.5$) for $Re = 10$, as shown in figure 24(c). When the Reynolds number jumps from 10 to 50, the bubble deforms more and develops sharp edges (figure 24e), with the aspect ratio of the now ellipsoidal bubble having increased from 1.97 to 2.73; a strong wake is observed behind the bubble with a length

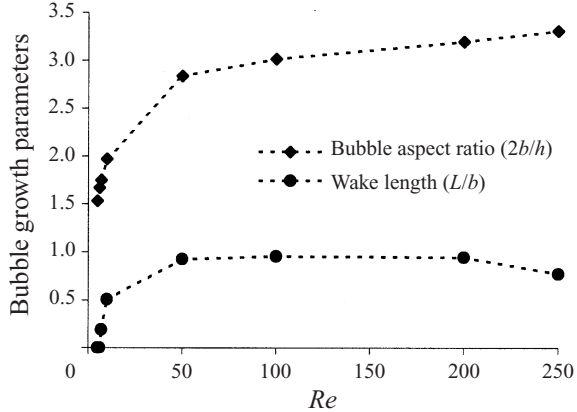


FIGURE 24. Bubble aspect ratio and wake length as a function of Reynolds number for the cases shown in figure 23.

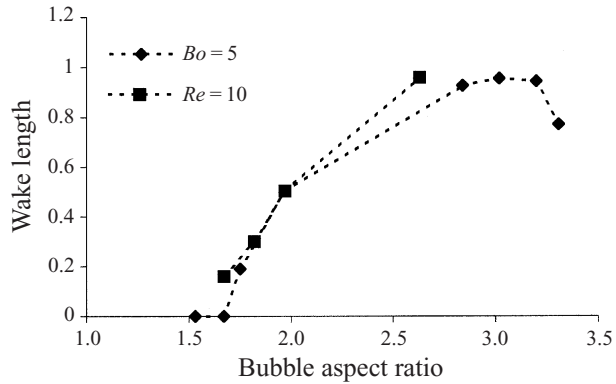


FIGURE 25. The relationship between bubble aspect ratio and wake formation for oblate-ellipsoidal and ellipsoidal-cap bubbles.

L/b of 0.93. With a further increase in Re to 100, the ellipsoidal bubble becomes flatter, with an aspect ratio of 3.02 and a slightly convex rear surface. The wake has grown stronger and more extensive, as may be seen in figure 24(f), with the length of the wake now standing at 0.956. When the Reynolds number is doubled to 200, the bubble becomes even more flattened, but with a slightly ragged edge, which may be attributed to the violent velocity field (figure 24g). Small bubbles begin to pinch off at the edge of the bubble, which has an aspect ratio of 3.2. The wake expands slightly in width, but its length has reduced to 0.945. For the largest Reynolds number studied of 250, the aspect ratio of the bubble increases further to 3.31; however, the length of the wake has reduced significantly to L/b of 0.772 (figure 24h).

The results for the aspect ratio of the ellipsoidal-cap bubble and the lengths of the wake formed as a function of the Reynolds number are summarized in figure 24. The formation of a wake depends on the final shape of the bubble, which in turn is determined by the fluid properties and initial bubble size. For a (deformable) bubble rising in a viscous liquid, a wake can occur only when the curvature of an ellipsoidal bubble is sufficient to accumulate enough vorticity. The bubble continues to increase in curvature with an increase in Re (for fixed $Bo = 5$), and the present simulations

show that for an ellipsoidal-cap bubble, the critical bubble aspect ratio for a wake to be formed is 1.75. However, for an oblate-ellipsoidal bubble resulting from a very low Bond number which travels faster than the ellipsoidal-cap bubble of the same aspect ratio, a wake can form at an aspect ratio as low as 1.67 (figures 21a and 25). Figure 25 summarizes the relationship between wake formation and bubble aspect ratio.

Predictions of wake formation and its relationship to bubble shape from the present study are consistent with studies in the literature. The flattened-ellipsoidal shape with sharp edges attained by the bubble at high Reynolds numbers agrees with the experiments of Wegener & Parlange (1973). The occurrence of a wake behind an oblate-ellipsoidal bubble for an aspect ratio as small as 1.67 in the present study supports the findings of Dandy & Leal (1986), who predicted the existence of a wake for the smallest aspect ratio considered in their study (defined differently from the present work, as major-to-minor axis ratio) of 1.60. However, the wake from our computations is much weaker than that predicted by Dandy & Leal; the wake lengths (L/b) in our study, which do not exceed a value of 1, are more consistent with those of Blanco & Magnaudet (1995), who found the maximum length of the wake to be 1.1. Since both Dandy & Leal and Blanco & Magnaudet studied bubbles of fixed shape which were not allowed to deform, and in view of the different non-dimensional parameters adopted in this study, no further quantitative comparisons between these sets of results is attempted. In fact, it is interesting to note that Blanco & Magnaudet (1995) pointed out the need for conducting studies on deformable bubbles as done in the present work.

It has also been shown here that the wake increases in size with an increase in Reynolds number, reaching a maximum value at a Reynolds number near 100; for $Re \geq 200$, the wake length decreases. This confirms the conjecture of Dandy & Leal (1986) that for a real, deformable bubble (unlike the fixed shape considered in their work), the wake would reduce in size with an increase in Reynolds number, and finally disappear at sufficiently high values. However, wake disappearance at high Reynolds numbers could not be verified with the present model since, as stated earlier, the bubble path would become oscillatory and the wake turbulent under these conditions, which would violate our assumptions. Our results do support the suggestion of Dandy & Leal that a wake can be formed at a finite Reynolds number for bubbles of any smooth shape, and that the mechanism for wake formation is the accumulation of vorticity.

5. Conclusions

The computations of the development of a bubble rising in a viscous liquid were carried out using a primitive-variables technique (SIMPLE), together with a modified VOF method. Although the method may not necessarily be superior to a variety of alternative numerical schemes available in the literature, the accuracy and the simple implementation of this algorithm are very attractive. The method developed in this study allows the study of the complex and highly transient formation of a toroidal bubble from an initially spherical shape. Instead of specifying a toroidal (e.g. Lundgren & Mansour 1991) or ellipsoidal (Dandy & Leal 1986, Blanco & Magnaudet 1995) geometry *a priori* as done in previous studies, we have simulated the entire process from the initial deformation of a spherical bubble to the formation of a toroid, including the development of a liquid jet below the bubble and its impact on the top surface of the bubble. We have also accounted for the effect of surface tension and viscosity of the liquid on the formation of the toroidal bubble, which was neglected by Best (1993) and Zhang *et al.* (1993).

The computed results have shown that as the effect of viscosity and surface tension increase, the impinging liquid jet beneath the bubble becomes broader and more diffuse until it can no longer penetrate the upper surface of the bubble; under such conditions, the bubble takes the shape of an elliptical cap or shell. During the process where the lower surface of the bubble contacts the upper surface, a higher surface tension results in multiple contact points leading to the formation of a small central bubble upon the impact of the liquid jet; this small bubble is centred on the axis of the larger, toroidal bubble. A number of smaller bubbles (also toroidal) detach from the lower extremities of the main bubble as it rises. It was found that when the Reynolds number reaches a value of 28 and the Bond number exceeds 20, toroidal bubbles are formed, and that with a further increase in Reynolds number, the base of the toroid becomes more spread out; the cross-section of the toroidal bubble also becomes more elongated with a decrease in surface tension. As the viscosity is decreased, the liquid jet bursting through the bubble impacts the supernatant liquid with a higher velocity. A toroidal bubble is always seen to travel more slowly than its elliptical or mushroom-shaped counterpart; moreover, a spherical-cap bubble rises faster than a skirted bubble. A higher density ratio results in a faster rise velocity. The transition from an elliptical-cap shape to a toroid occurs when the density ratio is greater than 5. For similar bubble shapes, the rise velocity increases with decreasing fluid viscosity and surface tension, and with increasing density ratio. The viscosity ratio does not have a significant effect on the motion or shape of the rising bubble. The conditions necessary for the formation of a trailing wake behind the bubble, as well as the characteristics of the wake formed, have also been investigated as a function of the bubble shape and fluid properties.

REFERENCES

- ANDERSON, C. R. 1985 A vortex method for flows with slight density variations. *J. Comput. Phys.* **61**, 417–444.
- BAKER, G. R. & MOORE, D. W. 1989 The rise and distortion of a two-dimensional gas bubble in an inviscid liquid. *Phys. Fluids A* **1**, 1451–1459.
- BEST, J. P. 1993 The formation of toroidal bubbles upon the collapse of transient cavities. *J. Fluid Mech.* **251**, 79–107.
- BHAGA, D. & WEBER, M. E. 1981 Bubbles in viscous liquids: shapes, wakes and velocities. *J. Fluid Mech.* **105**, 61–85.
- BLANCO, A. & MAGNAUDET, J. 1995 The structure of the axisymmetric high-Reynolds number flow around an ellipsoidal bubble of fixed shape. *Phys. Fluids* **7**, 1265–1274.
- BRACKBILL, J. U., KOTHE, D. B. & ZEMACH, C. 1992 A continuum method for modeling surface tension. *J. Comput. Phys.* **100**, 335–354.
- BRECHT, S. H. & FERRANTE, J. R. 1989 Vortex-in-Cell simulations of buoyant bubbles in three dimensions. *Phys. Fluids A* **1**, 1166–1191.
- CHEN, L., GARIMELLA, S. V., REIZES, J. A. & LEONARDI, E. 1997 Motion of interacting gas bubbles in a viscous liquid including wall effects and evaporation. *Numer. Heat Transfer A* **31**, 629–654.
- CHORIN, A. J. 1985 Curvature and solidification. *J. Comput. Phys.* **58**, 472–490.
- CHRISTOV, C. I. & VOLKOV, P. K. 1985 Numerical investigation of the steady viscous flow past a stationary deformable bubble. *J. Fluid Mech.* **158**, 341–364.
- CLAES, D. & LEINER, W. 1990 Computation of viscous free-surface flow around a single bubble. In *Proc. 8th GAMM-Conf. Numerical Methods in Fluid Mechanics* (ed. P. Wesseling), pp. 52–60.
- CLIFT, R., GRACE, J. R. & WEBER, M. E. 1978 *Bubbles, Drops and Particles*. Academic.
- DANDY, D. S. & LEAL, L. G. 1986 Boundary-layer separation from a smooth slip surface. *Phys. Fluids* **29**, 1360–1366.
- DAVIES, R. M. & TAYLOR, F. I. 1950 The mechanics of large bubbles rising through extended liquids and through liquids in tubes. *Proc. R. Soc. Lond. A* **200**, 375–390.

- DURAISWAMI, R. & PROSPERETTI, A. 1992 Orthogonal mapping in two dimensions. *J. Comput. Phys.* **98**, 254–268.
- FLORYAN, J. M. & RASMUSSEN, H. 1989 Numerical methods for viscous flows with moving boundaries. *Appl. Mech. Rev.* **42**, 323–341.
- FYFE, D. E., ORAN, E. S. & FRITTS, M. J. 1988 Surface tension and viscosity with Lagrangian hydrodynamics on a triangular mesh. *J. Comput. Phys.* **76**, 349–384.
- GLIMM, J., MARCHEZIN, D. & MCBRYAN, O. S 1981 A numerical method for two phase flow with an unstable interface. *J. Comput. Phys.* **39**, 179–200.
- HARTUNIAN, R. A. & SEARS, W. R. 1957 on the instability of small gas bubbles moving uniformly in various liquids. *J. Fluid Mech.* **3**, 27–47.
- HIRT, C. W. & NICHOLS, B. D. 1981 Volume of fluid (VOF) method for the dynamics of free boundaries *J. Comput. Phys.* **39**, 201–225.
- LAFOURIE, B., NARDONE, C., SCARDOVELLI, R., ZALESKI, S. & ZANETTI, G. 1994 Modelling merging and fragmentation in multiphase flows with SURFER. *J. Comput. Phys.* **113**, 134–147.
- LEVEQUE, R. J. & LI, Z. 1994 The immersed interface method for elliptic equations with discontinuous coefficients and singular sources. *SIAM. J. Numer. Anal.* **31**, 1019–1044.
- LUNDGREN, T. S. & MANSOUR, N. N. 1991 Vortex ring bubbles. *J. Fluid Mech.* **224**, 177–196.
- MAGNAUDET, J., RIVERO, M. & FABRE J. 1995 Accelerated flows past a rigid sphere or a spherical bubble. Part 1. Steady straining flow. *J. Fluid Mech.* **284**, 97–135.
- MARTEN K., SHARIFF, K., PSARAKOS, S. & WHITE, D. J. 1996, Ring bubbles of dolphins. *Sci Am.* August, 83–87.
- MEIJERINK, J. A. & VORST, H. A. VAN DER 1997 An iterative solution method for linear systems of which the coefficient matrix is a symmetric M-matrix. *Maths Comput.* **31**, 148–162.
- MOORE, D. W. 1959 The rise of a gas bubble in a viscous liquid. *J. Fluid Mech.* **6**, 113–130.
- MULDER, W., OSHER, S. & SETHIAN, J. A. 1992 Computing interface motion in compressible gas dynamics. *J. Comput. Phys.* **100**, 209–228.
- MURRAY, B. T., WHEELER, A. A. & GLICKSMAN, M. E. 1995 Simulations of experimentally observed dendritic growth behaviour using a phase-field model. *J. Cryst Growth* **154**, 386–400.
- NOH, W. F. & WOODWARD, P. R. 1976 SLIC (Simple Line Interface Calculation). In *Proc. 5th Intl Conf. on Numerical Methods in Fluid Dynamics* (ed. A. I. van de Vooren & P. J. Zandbergen). Lecture Notes in Physics, vol. 59, pp. 330–340. Springer.
- OGUZ, H. N. & PROSPERETTI, A. 1989 Surface tension effects in the contact of liquid surfaces. *J. Fluid Mech.* **203**, 149–171.
- PARTOM, I. S. 1987 Application of the VOF method to the sloshing of a fluid in a partially filled cylindrical container. *Intl. J. Numer Meth Fluids* **7**, 535–550.
- PATANKAR, S. V. 1980 *Numerical Heat Transfer and Fluid Flow*. Hemisphere.
- PEDLEY, T. J. 1968 The toroidal bubble. *J. Fluid Mech.* **32**, 97–112.
- PESKIN, C. S. 1977 Numerical analysis of blood flow in the heart. *J. Comput. Phys.* **25**, 220–252.
- PUCKETT, E. G. 1991 A volume of fluid interface tracking algorithm with applications to computing shock wave rarefaction. In *Proc. 4th Intl Symp. on Computational Fluid Dynamics*, pp. 933–938.
- RHIE, C. M. & CHOW, W. L. 1983 Numerical study of the turbulent flow past an airfoil with trailing edge separation. *AIAA J.* **21**, 1525–1532.
- RIDER, W. J., KOTHER, D. B., MOSKO, J. & CERUTTI, J. H. 1995 Accurate solution algorithms for incompressible multiphase flows. *AIAA Paper 95-0699*, pp. 1–17.
- RYSKIN, G. & LEAL, L. G. 1984 Numerical solution of free-boundary problems in fluid mechanics. Parts 1,2,3. *J. Fluid Mech.* **148**, 1–17; 19–35; 37–43.
- SETHIAN, J. A. 1985 Curvature and the evolution of fronts. *Commun Math. Phys.* **101**, 487–499.
- SETHIAN, J. A. 1996 *Level Set Methods*. Cambridge University Press.
- STONE, H. A. 1968 Iterative solution of implicit approximations of multidimensional partial differential equations. *SIAM J. Numer. Anal.* 530–590.
- STONE, H. A. & LEAL, L. G. 1989 Relaxation and breakup of an initially extended drop in an otherwise quiescent fluid. *J. Fluid Mech.* **198**, 399–427.
- SUSSMAN, M., SMEREKA, P. & OSHER, S. 1994 A level set approach for computing solutions to incompressible two-phase flow. *J. Comput. Phys.* **114**, 146–159.
- SWAMINATHAN, C. R. & VOLLMER, V. R. 1993 On the enthalpy method. *Intl J. Numer. Meth. Heat Fluid Flow* **3**, 233–244.

- TAYLOR, T. D. & ACRIVOS, A. 1964 On the deformation and drag of a falling viscous drop at low Reynolds number. *J. Fluid Mech.* **18**, 466–476.
- UDAYKUMAR, H. S., SHYY, W. & RAO, M. M. 1994 ELAFINT – A mixed Eulerian-Lagrangian method for fluid flows with complex and moving boundaries. *AIAA Paper 94-1996*.
- UNVERDI, S. O. & TRYGGVASON, G. 1992a A front-tracking method for viscous, incompressible, multi-fluid flows. *J. Comput. Phys.* **100**, 25–37.
- UNVERDI, S. O. & TRYGGVASON, G. 1992b Computations of multi-fluid flows. *Physica. D* **60**, 70–83.
- WALTERS, J. K. & DAVIDSON, J. F. 1962 The initial motion of a gas bubble formed in an inviscid liquid. Part 1. The two-dimensional bubble. *J. Fluid Mech.* **12**, 408–417.
- WALTERS, J. K. & DAVIDSON, J. F. 1963 The initial motion of a gas bubble formed in an inviscid liquid. Part 2. The three-dimensional bubble and the toroidal bubble. *J. Fluid Mech.* **17**, 321–336.
- WEGENER, P. P. & PARLANGE, J. Y. 1973 Spherical-cap bubbles. *Ann. Rev. Fluid Mech.* **5**, 79–100.
- WELCH, J. E., HARLOW, F. H., SHANNON, J. P. & DALY, B. J. 1966 The MAC Method: A computing technique for solving viscous, incompressible, transient fluid-flow problems involving free surfaces. *Los Alamos Sci. Lab. Rep.* LA-3425.
- YOUNGS, D. L. 1982 Time-dependent multi-material flow with large fluid distortion. In *Numerical Methods for Fluid Dynamics* (ed. K. W. Morton & M. J. Baines), p. 273. Academic.
- YOUNGS, D. L. 1984 Numerical simulation of turbulent mixing by Rayleigh–Taylor instability. *Physica* **12D**, 32–44.
- ZHANG, S., DUNCAN, J. H. & CHAHINE, G. L. 1993 The final stage of the collapse of a cavitation bubble near a rigid wall. *J. Fluid Mech.* **257**, 147–181.